The Role of Nanofillers in Polymer Nanocomposites

A Dissertation Presented

by

Di Xu

to

The Graduate School

in Partial Fulfillment of the

Requirements

for the Degree of

Doctor of Philosophy

in

Materials Science and Engineering

Stony Brook University

August 2016

Stony Brook University

The Graduate School

Di Xu

We, the dissertation committee for the above candidate for the

Doctor of Philosophy degree, hereby recommend

acceptance of this dissertation.

Dilip Gersappe – Dissertation Advisor
Professor, Department of Materials Science and Engineering

Miriam Rafailovich - Chairperson of Defense
Professor, Department of Materials Science and Engineering

Jonathan Sokolov
Professor, Department of Materials Science and Engineering

Robert B. Grubbs
Professor, Department of Chemistry, Stony Brook University

This dissertation is accepted by the Graduate School

Nancy Goroff
Interim Dean of the Graduate School

Abstract of the Dissertation

The Role of Nanofillers in Polymer Nanocomposites

by

Di Xu

Doctor of Philosophy

in

Materials Science and Engineering

Stony Brook University

2016

Polymer nanocomposites have been widely used in many fields. By introducing nanoparticles as fillers, researchers are able to get reinforced materials and new materials with novel properties, such as stronger mechanics, enhanced optical properties and improved conductivity. Though experimental techniques have rapidly advanced to enable better control of materials at atomic level, there is still a lack of a fundamental understanding of the dynamics and structure-properties relations in polymer nanocomposites. In this thesis, we use computer simulations to study the molecular structure and connections between microstate to macro properties of a variety of nanocomposites. Our goal is to understand the role of nanofillers in complex nanocomposite systems and to assist nanocomposite design.

Nanoplatelet fillers, such as clays, have shown superior effects on the properties of polymer gels. We used molecular dynamic simulation to study nanoplatelet-filled composite gel system, in which short-range attraction exists between the polymer and nanoplatelet fillers. We show that the polymers and nanoplatelet fillers formed organic-inorganic networks with nanoplatelets acting as crosslink junctions, and the network eventually percolates the system as fillers reached a critical concentration. Stress auto-correlation and step-strain test were applied to investigate the mechanical properties; the results show the simulated composites changed from fluid-like to solid-like. The mechanical changes were consistent with the percolation transition, and gelation mechanism was therefore believed to be similar to those pure polymer physical gels. It was observed platelets aggregated into a local intercalation structure, which significantly differs from typical spherical fillers. This unique intercalation structure was examined by radial distribution function and ordering parameters. We discussed how intercalation would affect the properties of the platelet composites by comparing them with spherical fillers.

Nanofillers have been widely used in polymer blends to improve the interfacial compatibility of otherwise immiscible polymers. In the second system, we investigated the interfacial behavior of binary polymer blends with different types of fillers. The interfacial tension and shear resistance were studied as a function of filler-polymer interaction, filler concentration and species of fillers. We found filler-polymer interaction is the key factor to improve the interfacial compatibility. The results show that nanofillers reduce both interfacial tension and interfacial slip at strong filler-polymer interaction. The effects of nanofillers however differ significantly from each other by their shapes. We analyzed the structure of nanofillers at the interface and their effects on the interfacial behaviors.

The self-assembly of polymers into a columnar structure, while subject to a thin film environment, provides an economic route to fabricate polymer solar cell (PSC) with high conversion efficiency. In our work, we showed that two immiscible polymer segregates into to a percolating columnar structure when confined to a thin film. By adding nanofillers, with specific functionality, we can template the segregation of nanofillers to the polymer-polymer interface. We prove this process is surface tension driven and is a result that is particular for thin film geometries, where the thickness is under critical value. The results provide a theoretical basis for the column structure forming in a self-assembled PSC system, and can help to select polymer candidates that optimize PSC efficiency. These studies serve as theoretical guideline for engineering novel nanocomposites, and could lead to the design of materials with new and improved properties.

Table of Contents

List of Figures

List of Table

List of Abbreviations

CMCS: Carboxymethyl chitosan
DFT: Density Functional Theory
FENE: Finite extensible non-elastic
KG: Kremer-Grest molecular simulation model
LAMMPS: Large-scale Atomic/Molecular Massively Parallel Simulator
LJ: Lennard Jones
MC: Monte Carlo
MD: Molecular Dynamics
NC: Nanocomposite
PC: Polycarbonate
P3HT: Poly(3-hexylthiophene)
PCBM: Phenyl-C61-butyric acid methyl ester
PS: Polystyrene
PSC: Polymer solar cell
PMMA: Poly(methyl methacrylate)
PNIPA: Poly(N-isopropylacrylamide)
PVA: Polyvinyl alcohol
SAC: Stress auto-correlation
SANS: Small-angle neutron scattering

Acknowledgments

I’d like to thank my advisor, professor Dilip Gersappe, for his constant support on my research and study. Thanks to professor Miriam Rfailovich for bringing many research ideas. Thanks to people in my group, Ning Sun, Jiaolong Jiang and Joseph N’Ortiz, we had a lot of fruitful discussions on researches. And thank you, my family and friends.

Publications

Di Xu; Divya Bhatnagar; Dilip Gersappe; Jonathan C. Sokolov; Miriam H. Rafailovich; Jack Lombardi. “Rheology of Poly(N-isopropylacrylamide)–Clay Nanocomposite Hydrogels”. *Macromolecules*, 2015, 48 (3), pp 840–846.

Cheng Pan; Hongfei Li; Bulent Akgun; Sushil K. Satijia; Yimei Zhu; Di Xu; Joseph Ortiz; Dilip Gersappe; Miriam H. Rafailovich. “Enhancing the Efficiency of Bulk Heterojunction Solar Cells via Templated Self-Assembly”. *Macromolecules*, 2013, 46 (5), pp 1812–1819

Chapter 1. Introduction

Polymers are large molecules made up of covalently bonded elementary units. The understanding and synthetic methodology of polymers have been rapidly developed and expanded since the fundamental theories of polymers were established in 1930-60s.[1-2] The chemical nature of polymers can be easily modified, e.g. by chemical grafting. The properties of polymer products can also be easily tuned by controlling polymer molecular weight, fabrication conditions and in many other ways. These features made polymer-based materials potentially a material of choice in many novel fields as well as a replacement to traditional metallic materials. Nowadays, polymers play a crucial role in many fields; polymers are widely used in biomedicine, such as in drug delivery and scaffold;[3] in clean energy, such as fuel cells and solar cells;[4-5] in aerospace[6] etc. Advances in polymer science have been accelerated as latest characterization methods have enabled researchers to study polymers at smaller and more accurate scales. In addition, modern computer simulations provide another innovative way to investigate polymer systems.

1.1 Polymer Nanocomposites

Adding organic or inorganic fillers to polymers has become a very common way to modify or reinforce the properties of polymeric materials. In the past 30 years, polymer composites with nanofillers have drawn extraordinary attention. Nanofillers are special type of fillers that has at least one dimension at a length scale of a nanometer.[7] The extraordinarily small size of the fillers result in nanoparticles with a high specific area and with large surface exposed to the polymer matrix. Nanoparticles are therefore very effective in improving the properties of polymers and have been widely used as fillers for many polymer composites. Based on their morphology, nanoparticles can be categorized into nanospheres, nanofibers and nanoplatelets. The structure of these fillers differ significantly from each other, the effects of them on the polymers are therefore have to be studied case by case.

Nanoparticles of spherical shape are the most common Nanofillers. Many studies show spherical nanoparticles can improve the performance of polymer and can be used to synthesize polymer composite with novel property. One example is adding nano SiO_2 to polymers, such as epoxy, can significantly improve the mechanical and thermal properties of the polymers.[8] By in situ process carboxymethyl chitosan (CMCS) with gold nanoparticles, a biocompatible nano composites with great potential as biosensor has also been achieved.[9] The dispersion state of spherical nanofillers usually has great impact on the properties of the nanocomposites. In a bilayer poly(methyl methacrylate) (PMMA) and polypyrrole blends, adding Fe_3O_4 nanoparticles could achieve a superparamagnetic response of the nanocomposite, but the effect is limited to uniform dispersion of Fe_3O_4 nanoparticles.[10] Another study compared the physical aging and glass transition of polystyrene, PMMA and poly(2-vinylpyridine) nanocomposites containing 10-15 nm silica nanospheres and 47 nm diameter alumina nanospheres, they found these two properties also depend greatly on the dispersion state of the nanofillers.[11]

Nanofibrous fillers, such as carbon nanotubes, Ag nanowires and etc, are another common type of nanofiller.[12] This type of nanofiller can usually be treated as nanowire of certain flexibility that can be bent to a limited degree. Nanofibrous fillers have shown great potential for materials of innovative properties. In one recent study, scientists developed a stretchable heater by using nanocomposite of silver nanowires and thermoplastic elastomer; they applied this nanocomposite to a wearable band as a thermal therapy for treating joint injuries.[13] Similar to spherical fillers, the dispersion state of nanofibrous fillers has strong impact on the performance of the composites. In a series of nanocomposites with surface treated carbon nanofibers, studies show a strong nanofiber-polymer adhesion is the key factor to improve the tensile strength and modulus of the product.[14] Nanofibrous fillers could also form network structures, studies show carbon nanotubes could be effective flame-retardant additives if they form a network structure in the polymer matrix. This is universal for many carbon-based nanoparticles such as single or multiwall carbon nanotubes, and carbon nanofibers.[12,15]

Nanoplatelet fillers, or nanosheet fillers, is another type of filler that usually has thickness about several to tens nanometers and diameter from tens nanometer to thousands nanometers. Nanoplatelet fillers show extraordinary effects on the mechanical performance of polymers. Studies show 0.05 wt% graphene can increase the glass transition temperature (T_g) of PMMA by 30 °C, the modulus and tensile strength of PMMA are also significantly improved.[16] By simple emulsion polymerization, researchers synthesized polystyrene-Na^+-montmorillonite nanocomposite that has significantly improved thermal stability and modulus.[17] Nanoplatelet fillers can also be applied to polymers to achieve novel properties. By in-situ polymerization of styrene with expanded graphite, researchers synthesized polystyrene-graphite nanocomposite that has high conductivity with graphite loading as low as 2.8-3.0 *wt*%.[18] Similar to the other two types of filler, the dispersion of nanoplatelet fillers plays an important role in many systems.[19]

1.2 Polymer Composite Gels

Gels are a special type of material that behaves between solid and liquid, Gels typically consists of two or more phases: a continuum phase, e.g polymer network, that defines the 'framework' to support the fixed structure of gels, and a dispersed phase, e.g. air or solvents, that fill the voids of the framework. Gels and networks are not strictly distinguishable, but networks usually refer to dry components while gels include a dispersed phase. Flory categorized gels into four types[2]:

1. Well-ordered lamellar structures, including gel mesophases.
2. Covalent polymeric networks; completely disordered.
3. Polymer networks formed through physical aggregation; predominantly disordered, but with regions of local order.
4. Particulate, disordered structures.

Some hybrid novel gels may not be well described by any of these types, e.g. composites gels may have both physical and chemical networks,[20] but these four types cover most polymer gels. In this thesis we are concerned particularly with physically crosslinked polymer networks using nanofillers as their crosslinking agent.

The behavior of polymer gels is determined by the physics of its internal continuum networks. Initial studies of gel physics during 1930-1960s were tightly connected to theories of rubber networks, and these quantitative works pioneered by Guth & Mark and Kuhn built the foundations for studying gels.[21-24] It is worth pointing out most of their theories treat networks as permanent linked ('chemically crosslinked' network), and extending these theories to physically connected gels obviously requires more effects to be taken into consideration, but they can serve as a starting point to formulate theories on physically connected gels. In both these cases, physical or chemical crosslinks, there is typically a transition zone where small local clusters evolve to a state of large percolated network.[25-26] Properties of the polymer start to change significantly above this transition zone, and solid behavior starts to dominate upon further crosslinking. Percolation and gelation is therefore almost indistinguishable, though there exist an active dispute among the community of whether percolation and gelation is the same thing.[27-28]

The networks in gel system are typically irregular and heterogeneous; theories to study the mechanics of gels therefore usually employ simplified models, such as the affine model and the phantom model.[1,29] These models are of significant value as a qualitative guideline in studying the mechanics of network and gels. The affine model assumes the crosslink junction is fixed in space while the phantom model assumes a flexible crosslink junction.[24-25,29-30] These two models are believed to predict the upper and lower limit of pure polymer networks, without considering the entanglements. There are many theories on polymer networks that were proposed based on these two theories. Head et al. studied the deformation of network of stiff filaments and they found distinct affine region and non-affine region depending on crosslink density and chain rigidity.[31] Candau studied the swelling and elasticity of polyelectrolyte gels, and deviations from the affine prediction were discussed.[32] Rubinstein and et al. analyzed the non-affine behavior of polymer networks, and constructed their model (modification of affine and phantom model) which depicted stress-strain behavior with excellent agreement with experiments.[33]

Applications of polymer gels could be significantly enhanced by including additional components. A common method has been adding nanofillers to synthesize polymer composite gels. For instance, nanospherical fillers, synthesized by grafting polymer to macromolecule microspheres (eg. polystyrene), could be used to fabricate polymer composite gels with high strength.[34] Nanoplatelet filler, such as clay, is one of the most popular nanofillers in hydrogel research. Haraguchi et al. synthesized a series of clay-enhanced hydrogels that have superior mechanical properties even compared to chemically crosslinked polymer hydrogels.[35] Mehrdad Kokabi et al. synthesized polyvinyl alcohol (PVA)–Clay composite gel that meet essential requirements for a wound dressing.[36]

1.3 Anisotropic Nanofillers

Adding nanofillers to polymers leads to enhancements due to large specific surface area of the nanofillers, but the properties of nanocomposites are affected by many other factors. Researchers have found degree of mixing between nanofiller and polymer matrix has strong effects on the final properties of the nanocomposite. Typically, the properties of polymer are better enhanced if nanofiller has stronger binding to it, weak adhesion between filler and polymer can results in materials failure due to interfacial tear off. The dispersion of fillers is another factor that impact the properties. It is related to the interfacial binding of filler and polymer but also affected by the fabrication process. Severely aggregated fillers can even degrade the properties of the polymers.[11,14] Polymers with anisotropic nanofillers are, particularly, strongly affected by the dispersion state of fillers.[14,19]

Nanoplatelet particles, such as clay, are widely used in polymer composites and colloids. The unique disk shape results in several interesting structures that have been revealed by experimental characterizations and simulations.[37-39] As in Figure 1a, layered nanofiller can randomly dispersed in the matrix uniformly, referred as exfoliated; or several layers can be bind together to form stacked state, e.g. by depletion force from the matrix, as Figure 1b; or several layers can bind together with polymers sandwiched between them, as Figure 1c, referred as intercalation state; layered silicates can also form a so called house-of-card state, in which the rim of the filler stand on the surface of other fillers, this state is more often observed in colloid system where fillers have opposite charges at rim and center. These different dispersion states can have a great impact on the properties of the nanocomposites; studies therefore have been extensively trying to determine the controlling parameters of these dispersions.[40] In particular, filler and solvent charges, size and dimension of the filler, and interactions between filler and matrix are some of the most common factors we are seeking to use to control the dispersion states of platelet fillers.

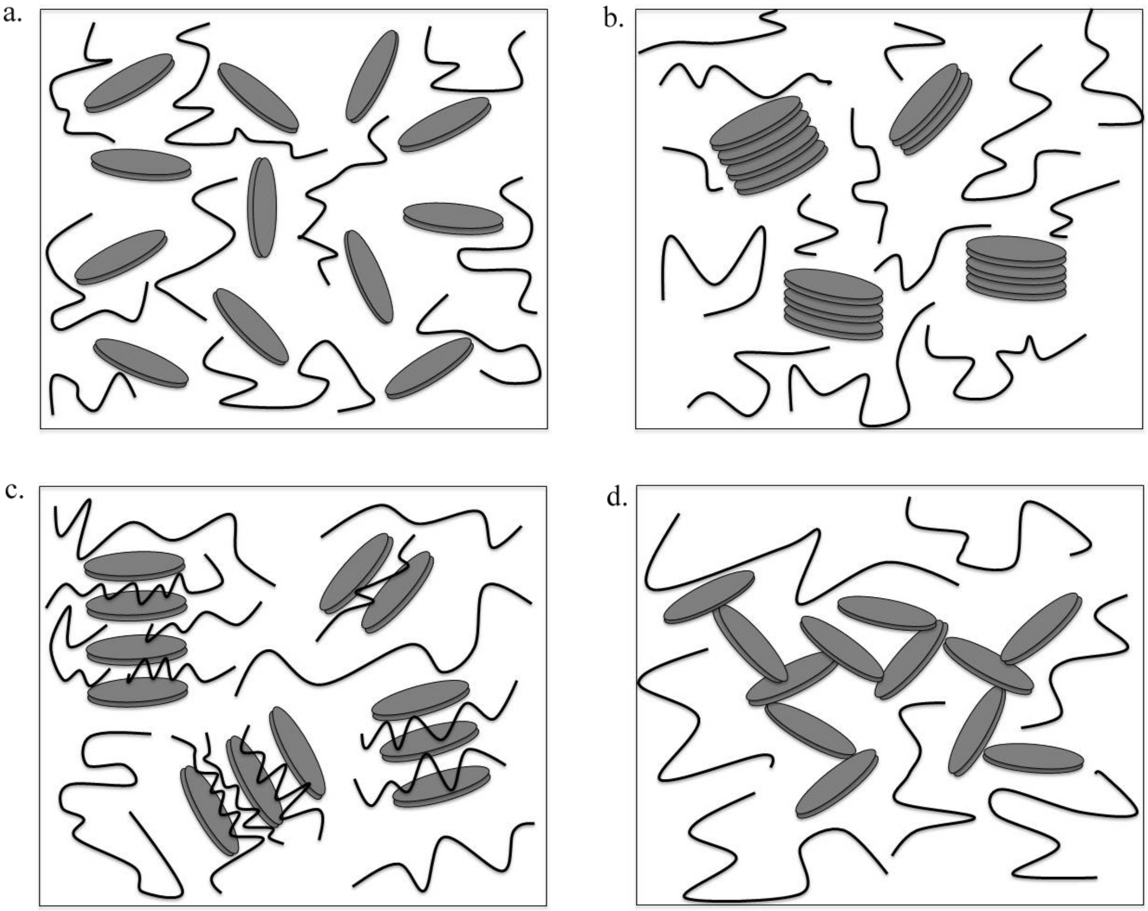

Figure 1. Four types of structure of clays in polymers/solvents. (a). Exfoliated; (b). Stacked; (c). Intercalated; (d). “House-of-Cards”.

The dispersion of nanofibrous fillers is affected by factors similar to those of nanosphere and nanoplatelet fillers. Nanofibrous fillers have diameter from several to tens nanometers, but the length of it can extend to hundreds or even thousands of nanometers. The flexibility of the nanofibrous fillers is another unique factor that impact the dispersion and the properties. Even rigid nanofibrous fillers can bend to a certain degree due to its long length. Nanofibrous fillers can form jammed networks or lamellar structure at certain conditions.[41-42] The dispersion and reinforcements is also affected by other details of the fillers, e.g. single wall carbon nanotube and multi wall carbon nanotube can have significant different effects on same polymer matrix.[43-44]

In this thesis, we concentrated on three material systems; nanocomposite hydrogel, polymer blends with nanofiller compatibilizer and polymer composites in polymer solar cells. We investigated the molecular structure of polymers and nanofillers for these systems while focusing on fundamental factors that can significantly change the behavior of these systems. We analyzed different kinds of fillers and their shape in order to connect the structure to property relations of these composites. The results of our study can provide theoretical guidelines to reinforce polymer systems and to invent novel polymer materials with tailored properties.

Chapter 2. Molecular Dynamics Simulation

The advantages of simulations enable researchers to tackle otherwise unsolvable puzzles that require extensive calculations, are experimentally hazardous or simply too costly. Computer simulation is a computer-based research method that constructs abstract models of the real problem, calculates the theoretical equations and processes mathematical analysis. Applications of simulations exist in almost every field. For instance, manufacturing use simulations to guide inventories, weather station use simulations to predict future weather, fire department uses simulations to control forest fires and astronomy uses simulation to study hypothetical theories. Materials scientists, particularly, use a variety of simulation methods to study materials at all scales.

There are a few commonly used simulation methods in materials science. Density functional theory (DFT) is a quantum-scale modeling method that solves for the space-dependent electron density.[45] It is one of the most popular simulation methods in condensed physics and computational chemistry. Molecular dynamic simulation is a molecular level simulation method that simulates interactions of atoms or united-atoms.[46] At the micron level, wider choices of simulation methods are available, finite element or finite volume methods are frequently used in fluid dynamics,[47-48] and the Lattice Boltzmann model is suitable for complex geometrical systems.[49] Simulation methods are picked primarily according the scope of the problem to be studied. Other factors include the purpose of the study and computation efficiency. For our purposes, we focused on molecular dynamic simulation. We introduce our model in the following sections and details of the model are further described in later chapters.

2.1 MD Simulation Basics

The microstate of a classical system can be described by the position and momentum of particles. By assuming Born-Oppenheimer approximation, the electron motions can be excluded.[46,50] The microstate of a particle system can be described by a Hamiltonian equation of the form:

$$\mathcal{H}(r,p) = \mathcal{K}(p) + \mathcal{V}(r) \tag{1}$$

The Hamiltonian function uses generalized coordinates r and momentum p of each atom, and uses simple additive form of the kinetic energy $\mathcal{K}$ and potential energy $\mathcal{V}$. Given an appropriate potential $\mathcal{V}$ that describe intermolecular interactions, entire time-evolution of particle motions and all properties of the system is achievable by writing down the Hamiltonian equations of state. This equation forms the theoretical basis of molecular dynamics simulation, which, in essence, solves this equation of atoms' motion.

In MD simulation, basic physical quantities follow a simple classical form. Consider an example of isolated system, which has fixed number of particles N and conserved total energy E. The velocity is simply the first derivative of position to time $v_i = \dot{r}_i$, the momentum $p_i = m\dot{r}_i$, force on particle *i* is the partial derivative of cumulated potential $F_i = -\frac{\partial \mathcal{V}}{\partial r_i}$. Kinetic energy take the simplest form $\mathcal{K} = \sum_{i=1}^{N} \sum_{\alpha} p_{i\alpha}^2 / 2m_i$, here α is the directions of the simulated system (*x*, *y* and *z* in a 3d simulation). With all these basic quantities, statistical mechanics provide a path to get macro state properties.

Proper potential fields are one of the key factors that determine the quality of MD simulation. For a system containing N atoms,

$$\mathcal{V} = \sum_i v_1(r_i) + \sum_i \sum_{j>i} v_2(r_i, r_j) + \sum_i \sum_{j>i} \sum_{k>j>i} v_3(r_i, r_j, r_k) + \cdots \tag{2}$$

The kinetic energy can be summed over a single term, a paired term and a triplet term. $v_1(r_i)$ typically accounts for external effects, e.g. Electrical fields on the system. The third term v_3 is triplets of molecules that contain three-body contribution to the total potential.[46,50] However, three-body (or any higher) are rarely used in MD simulation mainly due to the high computation intensity involved. On the other hand, pairwise approximation usually yields remarkably good results for simulations of many systems. Three-body interaction can also be partially integrated into pairwise terms and lead to the final form of potentials

$$\mathcal{V} \approx \sum_i v_1(r_i) + \sum_i \sum_{j>i} v_2^{eff}(r_{ij}) \tag{3}$$

Here, v^{eff} is the effective pairwise potential that actually used in most MD simulation. Eg, for an argon system, studies have used a simple Lennard-Jones 12-6 potential of the form[51]

$$V^{LJ}(r) = 4\varepsilon\left[\left(\frac{\sigma}{r}\right)^{12} - \left(\frac{\sigma}{r}\right)^{6}\right] \tag{4}$$

This potential has been proved to provide a remarkably good description of the properties of argon atoms with appropriate choice of parameters.[46,50]

Real MD simulation models usually includes a lot more steps, which include computing algorithms, model abstractions, and post processing.[52] Fortunately, MD simulation is a very mature technique and there are many useful books that give a through explanation of the manner in which to set up MD simulation models.[46,50,52-53] In the following sections, we selectively introduce some of the key methods in MD simulation that we think are crucial to our studies.

2.2 Verlet Time Integration Algorithm

Fundamental physical quantities, such as velocity, acceleration, and coordinates are the keys for solving Newton's equation of motion and therefore a core part of simulating particle dynamics. Finite difference method solves integration problems quite well and is often used to calculate particles' trajectory in MD simulation. Expanding the time dependent coordinates of a particle in a Taylor series,

$$r(t+\Delta t) = r(t) + \frac{dr(t)}{dt}\Delta t + \frac{1}{2}\frac{d^2r(t)}{dt}\Delta t^2 + \frac{1}{3!}\frac{d^3r(t)}{dt^3}\Delta t^3 + \cdots \tag{5}$$

An integration methods that neglects $(\Delta t)^{n+1}$ and higher terms is named as *n*th-order method with truncation error at n+1th. With this convention, a higher order integration method has smaller truncation error, but of course at the cost of computation time.

Verlet's algorithm is one of very commonly used finite-difference method that has a third order truncation error.[54] To write the Taylor series back by one step

$$r(t-\Delta t) = r(t) - \frac{dr(t)}{dt}\Delta t + \frac{1}{2}\frac{d^2r(t)}{dt}\Delta t^2 - \frac{1}{3!}\frac{d^3r(t)}{dt^3}\Delta t^3 + \cdots \quad (6)$$

adding these two equation and neglecting fourth order and higher terms, we get

$$r(t+\Delta t) = 2r(t) - r(t-\Delta t) + \frac{d^2r(t)}{dt}\Delta t^2 \quad (7)$$

The advantage of the method is that it's computationally more efficient, and has a smaller round off error. However, central difference estimation is further need to extract velocity from this method of integration.

Some additional simplification leads to the more widely used velocity-Verlet algorithm[55] with the form

$$r(t+\Delta t) = r(t) + v\Delta(t) + \frac{1}{2}a(t)\Delta t \quad (8)$$

$$v(t+\Delta t) = v(t) + \frac{1}{2}[a(t) + a(t+t\Delta)]\Delta t \quad (9)$$

This method actually involves two stages. Firstly, the new positions at time *t*+Δ*t* are calculated. The velocity at mid-step is then computed by

$$v\left(t+\frac{1}{2}\Delta t\right) = v(t) + \frac{1}{2}a(t)\Delta t \quad (10)$$

After the first step, the forces and accelerations at time *t*+Δ*t* are then computed, and the velocity updates is completed by

$$v(t+\Delta t) = v\left(t+\frac{1}{2}\Delta t\right) + \frac{1}{2}a(t+\Delta t)\Delta t \quad (11)$$

The velocity-Verlet algorithm is storage efficient, numerical stable and implementation convenient, it is perhaps the most popular time integration method in MD simulation and is also what we used for our simulation.

2.3 Simulation Ensembles

In most simulations, in addition to the local particle positions and velocities, we are also interested in macroscopic information, such as pressure, total energy, temperature and etc. Basic thermodynamic properties (number of particles, temperature and etc.) can be calculated from the microstate parameters (coordinates, momentum and etc.). By using statistical mechanics properly for different ensembles, we are able to further extract information what we are indeed interested in. In conventional statistical mechanics, an ensemble average is typically used to calculate thermodynamic properties.[46,50] Let $\Gamma(t)$ be a collection of particles at time t, it then represents a particular state of the phase space. The particles follow a distribution according to a probability density $\rho(\Gamma)$. The equilibrium ensemble $\rho_{\text{ens}}(\Gamma)$ can be proved to be time independent, because once a system leaves $\Gamma(t)$ and move to $\Gamma(t+1)$, another system arrives at $\Gamma(t)$ from $\Gamma(t-1)$. Let $\mathcal{A}$ be some property of interest, it follows the relations that

$$\mathcal{A}_{obs} = \langle\mathcal{A}\rangle_{ens} = \langle\mathcal{A}|\rho_{ens}\rangle = \sum_{\Gamma}\mathcal{A}(\Gamma)\rho_{ens}(\Gamma) \tag{12}$$

Ensemble average is therefore always replaced by trajectory average, or called time average, which is the average of $\mathcal{A}(\Gamma(t))$ by

$$\mathcal{A}_{obs} = \langle\mathcal{A}\rangle_{ens} = \frac{1}{n_{obs}}\sum_{i=1}^{n_{obs}}\mathcal{A}(\Gamma(t_i)) \tag{13}$$

in the equation, n_{obs} is the number of observations we take in simulation. t_{i} is the time of i th observation. This equation offers the convenience for extracting thermodynamic properties in MD simulation since the simulation evolves step by step for a fixed time length.

The detailed prescriptions for calculating thermodynamic properties vary from different ensembles, e.g. canonical ensemble (NVT) and micro-canonical ensemble (NVE). Many textbooks give clear explanations that cover almost every kind of ensemble that would be encountered.[46,50,52-53,56] We refer the reader to these textbooks to find how physical properties and thermodynamic quantities are calculated. But the validity of time average and MD results lies on some additional conditions, as M.P Allen pointed out in his textbook, first, the probability density should not change; second, the stationary state has to be reachable for any reasonable starting distribution; third, the system should be ergodic.[46] Empirically, simulations from different starting states should leads to similar results.

2.4 Reduced units

Different unit bases can be used in MD simulations. Real units can be used in MD simulation, for which distance typically has the unit of angstroms, temperature is in Kelvin and so on. Standard International Units are also used sometimes, for which mass is in kilograms, distance in meters. And there are many more units we found in literatures of MD simulation. Although the results of an MD simulation is invariant to the units it uses, the units should be selected carefully to fit the problem being studied. It is also very important to understand the unit being used in MD simulation (or almost in every computer simulation) in order to interpret the results correctly.

Reduced units are often used in computer simulations.[52] In reduced units, some referenced parameter is chosen as the unary basis, all the other parameters are then reduced into a unit-less form based on the selected references, the overall simulation therefore become dimensionless. There are many advantages in using reduced units in simulations. First, by using reduced unit, all parameters take values that are close to unary (eg. number of single digit), which could avoid round-off errors in calculations, e.g. representing nanometer values in meter could result in long decimal digits. Second, reduced units can save computing resource by integrating some calculation into units; e.g. in the Lennard Jones equation, if distance r is in reduced to the σ, we could save the step of dividing σ/r. Third, reduced units provide a convenient way to compare results from different systems that can be described by similar models.

We used reduced units in all of our simulation (also called LJ unit). The fundamental quantities mass m, sigma σ, epsilon ε, and Boltzmann constant are all set to 1 as the unary basis. All other quantities are reduced into dimensionless form. Using asterisk to denote the unitless quantity being used in our simulation, they hold a simple relation to the quantity in real units, for instance the

distance $x^* = \frac{x}{\sigma}$;

time $t^* = t * \left(\frac{\varepsilon}{m\sigma^2}\right)^{0.5}$;

energy $E^* = \frac{E}{\varepsilon}$;

velocity $v^* = v\frac{\tau}{\sigma}$;

force $f^* = f * \frac{\sigma}{\varepsilon}$;

temperature $T^* = T * \frac{K_b}{\varepsilon}$;

pressure $P^* = P * \frac{\sigma^3}{\varepsilon\tau}$;

All the quantities can be converted back to their real value accordingly.

2.5 Kremer-Grest Model

Extraordinary efforts are often required to truly validate MD models. As mentioned before, all thermodynamic quantities extracted from simulations require the system to be ergodic; this however is impossible to measure and is usually justified empirically by starting simulations from different initial conditions. Even coarse grained MD simulations are typically at the nanometer scale, and it is difficult to validate the model by directly comparing it with experimental results, as the time scales of MD simulations are much shorter. In the case of polymer simulations however, coarse grained MD models have been applied to polymer systems since the 1960s, and as a result models have been validated and widely used in studying polymer systems.[57]

Kurt Kremer and Gary S. Grest extensively explored some fundamental aspects of polymer physics by using molecular dynamic simulations in the 1990s.[57-64] They used a bead spring MD model to study Rouse and reptation behavior of polymer chains, polymer entanglements in melts and crosslinking in polymer melts. Their model was computationally efficient, theoretically simple, yet extensively proved by researchers as an excellent model for polymer physics studies. Their model, also called KG model, is one of the most popular coarse grained MD model in studying polymer physics. They used a simple Lennard-Jones potential for pairwise interactions,

$$V^{LJ}(r) = \begin{cases} 4\varepsilon\left[\left(\frac{\sigma}{r}\right)^{12} - \left(\frac{\sigma}{r}\right)^{6}\right], & r \le r_c \\ 0, & r \ge r_c \end{cases} \tag{14}$$

r_c is the cutoff distance, beyond which LJ potential was neglected. Kremer used a cutoff $r_c = 2.5\sigma$, as we could be seen from the potential curve of LJ equation, in Equation 14, pairs at distance farther than cutoff have negligible contribution to the total potential. The minimum LJ potential energy equals -ε at pair distance $2^{1/6}\sigma$.

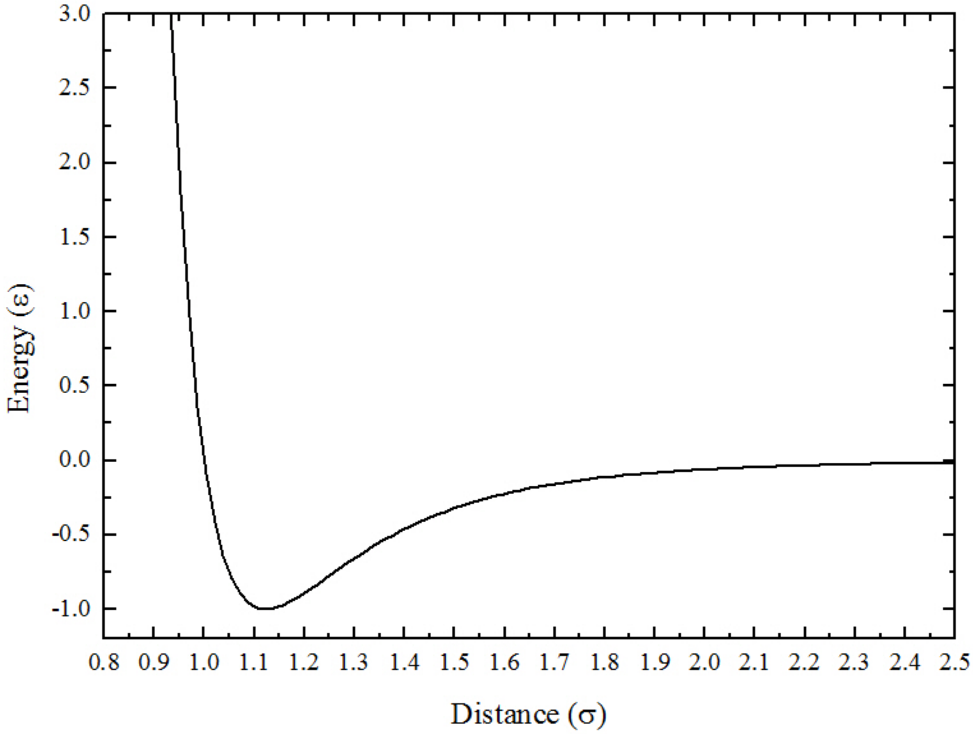

Figure 2. Lennard-Jones potential as a function of distance between paired particles. The potential reached minimum value $-\varepsilon$ at pair distance $2^{1/6}\sigma$.

In the KG model, the polymer chains are connected by the simple finite extensible nonlinear elastic (FENE) potential, which has the form

$$V^{bond}(r) = \begin{cases} 0.5R_0^2 k ln\left[1-\left(\frac{r}{R_0}\right)^2\right], & r \le R_0 \\ \infty, & r > R_0 \end{cases} \tag{15}$$

R_0 in the equation is the maximum extensible distance and k is the elastic constant. In the KG model, they used $k = 30\varepsilon/\sigma^2$, $R_0 = 1.5\sigma$ and $k_B T = 1.0\varepsilon$. The FENE potential combined with LJ potential is used to construct the overall bead-spring model of simple polymer system. Kremer and Grest proved the entanglement length (N_e), in simulated polymer melt of density $\rho = 0.85$, is approximately 35 segments (beads).[58,64] This simple generic model is good enough to capture the crossover from the Rouse model (polymer chain length that below N_e) to the reptation model (polymer chains that longer than N_e).[58] They also proved the model has a good description of polymer network system by careful comparison with rubber network theories.[61-62]

Our MD model follows the basic principles from the KG model, with some extensions to finite sized particles, and the addition of implicit or explicit LJ solvent. One difference that should be pointed out is that a Langevin thermostat is used to control the temperature T in original KG model,[57,65-66] however we use a Nose-Hoover thermostat and Nose-Hoover barostat.[66-67] In the Langevin method the friction effect of the solvent is used implicitly, and is therefore widely used in simulations involving Brownian motion. The Nose-Hoover method simply adds constraints to the momentum and coordinates of the simulated system. It projects the partition function to an extended system, and therefore doesn't alter the simulated ensemble. We used a damping factor of 100 simulation steps for thermostat and 1000 steps for barostat. Details about the Nose-Hoover can be found on LAMMPS website.[68] It's also worth to mentioning that in the original KG model, authors proved $\Delta t=0.012\tau$ is sufficiently accurate for the simulation, while we used even smaller step size that $\Delta t=0.005\tau$ for better precision.

2.6 LAMMPS Simulation Package

Large-scale Atomic/Molecular Massively Parallel Simulator (LAMMPS) is one of the most popular simulation packages in the market.[68-69] LAMMPS, while distributed by Sandia National Laboratories, has been developed by collaboration of many researchers from different fields. It is well accepted by material science community, chemical engineering community, condensed physics community, and the mechanical engineering community. LAMMPS works well for MD simulations from coarse-grained models to full atomistic models, and has been used in a lot of materials science research. LAMMPS is also easily extendable and well maintained by experts; the community has actively expanding it with new features, and has incorporated some of the latest techniques, such as GPU parallelization, to it. We used LAMMPS for all of our simulation in this thesis.

Chapter 3. Polymer Hydrogels With Nanoplatelet fillers

3.1 Introduction

Hydrogels are a class of material that due to their high water content, are inherently biocompatible. They have found a number of uses including drug delivery, soft robotics and tissue engineering.[36,70-72] In recent decades, the increasing demands for hydrogels of improved performance, especially in bioengineering, has promoted the development of nanocomposite hydrogels. The presence of nanoparticles could enhance the polymer matrix, such as to improve the mechanics, as well as introduce hybrid features, such as conductivity.[73-75] Among the variety of nanocomposite gels, those with disk-shape nanoplatelet fillers, typically silicate platelets, have draw a lot of attentions.[76-79] Nanoplatelet fillers have strong steric hindrance and offer large surface for polymer adsorption, and therefore generally offer the possibility of enhancing the strength of the gel. In some of the latest studies, graphene sheets have also been applied to synthesize novel gels in order to incorporate the unique properties of graphene.[80-81]

Haraguchi et al. did systematic studies on nanocomposite gels and soft polymer nanocomposites with clays.[35,73,77,82-95] They found disk-like clay platelets and monomers formed clay-brush particles during in situ polymerization and finally led to polymer/clay organic-inorganic networks.[89] This type of nanocomposite gel shows extraordinary optical, mechanical and swelling/deswelling properties.[93] Especially when concentration of clay was above a critical value, the elongation at break didn't further reduce with increasing clay concentration while the modulus significantly increased.[91] In contrast, a chemically crosslinked pure polymer gel (made of the same polymer) had a heterogeneous network structure, which resulted in brittle behavior due to defects. These studies showed polymers and clays formed a unique organic-inorganic network, and this structure had a major contribution to the enhanced properties of clay nanocomposite gels.

Clear understanding of the interplay between polymer and platelets is required in order to fabricate platelet filled nanocomposite gels of finely tuned properties. Advanced characterization techniques enabled us to get insights about the internal structure and dynamics. For example, small-angle neutron scattering (SANS) in PNIPA-clay gel gels revealed adsorption polymer layers wrapping around clays, and evidence of polymers that bridges clay units;[90] and dynamic light scattering measures shows thermal fluctuation of clays was suppressed upon gelation.[96-99] The theoretical studies of how nanoplatelet fillers improve the performance of gels, however, are still at their infancy. Computer simulations of nanoplatelet filled gels at molecular level are thus required and promise to provide a bridge between molecular structures and macro properties, and to provide guidance for studies on novel composite gels.

Although there are many simulations researches on clay colloids,[39,100] there is a lack of a well-established molecular model for nanoplatelets. The Monte-Carlo simulation of Dijkstra and et al., has used rigid thin disks to model clay platelets,[39] while more recent attempts of Delhorme and et al., used arranged spheres with dihedral constraints to form a single layer disk.[40,100] Ideally, the large aspect ratio of platelet fillers should be maintained in a simulation, this however requires the system to be large enough to eliminate effects that platelet might interact with itself across the simulation boundary. Further more, to investigate the infrastructure of the polymer networks formed in composite gel, this would require even larger simulation size. As a result, the size of the platelet has to be compromised in simulations of nanoplatelet-polymer composite gels.

In this study, we used a molecular dynamics model to study some of the fundamental issues of nanoplatelet filled composite gels. The end-monomers in the simulation interact with platelets by a short-range attraction force, which lead to the forming of a globally spanning organic-inorganic network at very low platelet loads. We looked into details of some classical aspects of polymer gels, such as the formation of percolating network, the dynamics of polymers as well as mechanical test of the composites. We also found platelets formed intercalated local structures that act as crosslinking nodes. This unique structure of platelets and the effects of such structure is analyzed and discussed. Our simulation is among the few that study composite gels with platelet fillers. The results of this generic model has predicted the molecular structures of nanoplatelet filled composite gels and cast light on how the structures would affect the overall mechanical properties of the composite gel.

3.2 Model and Methods

We used a molecular dynamics simulation model the same as described in chapter 2, it mainly adopted the KG model with some modifications. Reduced units were used by letting energy ε, distance σ, mass m and Boltzmann constant k_B to be unity. The simulation domain is a cubic box of fixed length 70.0σ. Standard periodic boundary is applied to all three dimensions (x, y and z) to minimize edge effects. We used the Verlet velocity integration method, as introduced in chapter 2, with a fixed step size of $\Delta t=0.005\tau$. Nose Hoover thermostat and barostat is used if needed, details on the environmental settings is introduced later in this section. All simulations are accomplished by using LAMMPS simulation package, with 24 CPUs of Handy cluster, at Institute for Advanced Computational Science (IACS), Stony Brook University.

3.2.1 Nanoplatelet Filler

Nanoplatelet fillers, particularly clays, have thickness about several to tens of nanometers, the diameter, however, could be hundred nanometers. A most ideal model would be a large simulation domain that encapsulates large platelets that has aspect ratio close to the real value. It means length of simulation box has to be at least a thousand sigma in order to simulate an ensemble with billions of particles, which is a great computational challenge. In our model, we simulate the nanoplatelet fillers by rigid bodies of specially arranged atoms, which capture the most significant characters of nanoplatelet fillers, such as large aspect ratio and anisotropic shape. The simplified nanoplatelet model enables us to simulate a large enough system to look at the global network structures in polymer gel system.

We use 19 spheres densely packed in a fcc(111) lattice to simulate each platelet, as in Figure 3. The exact shape is a hexagon plane, which is the closest shape to resemble a disk by using spherical particles. The simulated fillers have diameter 5.0σ and thickness 1.0σ, the aspect ratio (about 5) is still far smaller than the real value of clay or graphene, but it kept the asymmetric nature of platelets. Each platelet is treated as a rigid body with the shape conserved during simulation, the torque and force is aggregated at each simulation step from the 19 spheres, the platelet then updates its orientation and position. The number of platelets is the main parameter that being studied in this paper, the volume fraction ranges from 0-2.9% ($\phi=19*n\pi\sigma^3/6V$, n is the number of platelets and V is the volume), which is lower than the critical value for colloid gel formation reported. We thus need not to worry about the effects of colloid gelation given the small aspect ratio, low fraction of platelets and lack of long-range interactions presented in our simulations.

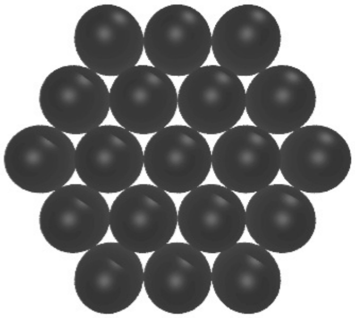

Figure 3. Model of nanoplatelet fillers used in simulation, each nanoplatelet consist of 19 spheres packed densely in hexagon lattice.

3.2.2 Potential Fields

The model used in this study has a minor change to the one introduced in Chapter 2. Polymers are simulated with an FENE potential of the form

$$V^{bond}(r) = \begin{cases} 0.5R_0^2kln\left[1-\left(\frac{r}{R_0}\right)^2\right], & r \leq R_0 \\ \infty, & r > R_0 \end{cases} \tag{16}$$

parameters of the FENE potential are the same as in the KG model, $R_0 = 1.5\sigma$ defines the maximum extensible length of the bonds, and $k = 30\varepsilon/\sigma^2$ is the spring constant. We simulate polymers with uniform length of 20 segments, this is far below the entanglement threshold. The number of polymer chains is kept constant at 4,000 chains in all simulations, corresponding to volume fraction about 12.2% ($\phi = 20n\pi\sigma^3/6V$, n is the number of chains and V is the volume). To allow physical bond formation, both end of the chain are labeled as sticker monomers that can potentially attract to fillers.

Lennard Jones (LJ) potential with cutoff is used for all pairwise interactions

$$V^{LJ}(r) = \begin{cases} 4\varepsilon\left[\left(\frac{\sigma}{r}\right)^{12}-\left(\frac{\sigma}{r}\right)^{6}\right], & r \leq r_c \\ 0, & r \geq r_c \end{cases} \tag{17}$$

the parameters of the equation are mostly the same as the origin KG model, ε and σ are all initiated to unit value. It should however be noted that a cut-off distance of r_c is set at 1.12σ for all pairwise LJ interactions, this value of r_c imposes purely repulsive force to all pairs. We used this cutoff value to simulate implicit good solvent condition for both polymers and fillers. The advantage of using implicit solvent is mainly to save computation cost, but it may lose some control on the solvent effects and hydrodynamics info.

3.2.3 Simulation Procedures

All simulations start from mixtures of nanoplatelet fillers and polymers using an implicit good solvent condition. The filler concentration varies from 0-2.9% as aforementioned, while the polymer concentration is always fixed. To exclude any dependency on the initial condition, we start from fillers and polymers randomly distributed in the simulation domain, and present results as an average over at least 3 simulations. The composite systems are pre-equilibrated for $5\times10^4\tau$ in NVT condition (T=1 if not otherwise mentioned). This step is required to minimize the energy to a reasonable value and to stabilize the motion to a reasonable amount, since the energy might fluctuate wildly due to the random initial condition that unavoidably has overlapping to some extent.

After pre-equilibration, polymer chains are uniformly dispersed in the simulation box, platelets are dispersed at exfoliated state of random orientations, with negligible small amount of stacking caused by the depletion force from polymers. The physical bondings are then switched on by setting ε_b equals to 5, and r_c equals to 2.5σ for the LJ potential between end-monomers and platelets. Studies of polymer physical gels have shown that physical gelation is sensitive to environmental temperature and bonding energy, as both terms affects the gelation bonds' lifetime and in turn affects the gelation behavior.[101-104] Our ε_b is chosen with preliminary simulations and referencing literatures on physical gel simulations.[105] The composites were further equilibrated after physical bonding was turned on. We equilibrate another $5\times10^4\tau$ for systems with 0-1.12*vol%* fillers, or $5\times10^5\tau$ for those with higher filler fraction to account for the slower dynamics for systems with higher filler concentration.

3.2.4 Analysis Methods

Mechanical properties of the polymer physical gel are one of the main interests of our study. On one hand, the abrupt change of mechanical properties signifies the transition from the liquid state to a solid, On the other hand, we are interested in how nanoplatelet fillers can reinforce the strength of polymer gel. We employed stress auto-correlation (SAC) and step-strain test as the main characterizations of the mechanical properties.[106-107] The stress auto-correlation is defined as

$$G(t) = \frac{V}{3k_BT}\sum_{\alpha\beta}\langle\sigma_{\alpha\beta}(t_0)\sigma_{\alpha\beta}(t_0+t)\rangle \tag{18}$$

G(t) is a function of delay time t, which could range from 0 to infinite. In the equation, V is the volume, T is the temperature, k_B is Boltzmann constant; σ is the stress tensor and $\alpha\beta$ denote the direction, we averaged three pressure tensors, xy, yz, and zx, in the equation for better precision.[50,106] Stress auto-correlation function is typically calculated as part of Green-Kubo method to calculate system viscosity in a static way (without disturbing the system).[50] The Green-Kubo method integrate stress auto-correlation by time to get viscosity, as

$$\eta = \int_0^{+\infty} G(t)dt \tag{19}$$

Discrete integration method is usually used in simulations. However, the time integration requires that stress auto-correlation function to decay to 0, which cost extraordinary long simulation time for gels of "solid-like" properties (The decay is extremely slow). We therefore employ only the stress auto-correlation function, part of the Green-Kubo formula. In this study, we use stress auto-correlation function with delay time t up to $1\times10^4\tau$, and time-averaged over $5\times10^4\tau$; the results turn out to be sufficient to qualitatively predict the trends of the viscosity changes.

Green-Kubo method requires the stress autocorrelation function to decay to zero, which requires a long simulation time.[108-109] We therefore used step-strain test, a non-equilibrium test, as a complementary method to stress autocorrelation function. In the step-strain test,[107] the simulation box is rapidly elongated by 100% in the x direction. The elongation is accomplished in 100τ with the volume conserved by contracting in the other two directions. All particles are carefully remapped into the new box without any extra velocities. The normal tension is calculated as function of delay time t of the form

$$\sigma(t) = \sigma_{xx} - 0.5(\sigma_{yy} + \sigma_{zz}) \tag{20}$$

the value of $\sigma(t)$ is calculated with t from 0 to $2.5\times10^4\tau$. These two tests have been proved, in entanglement polymer system, could be related by some damping factor.[107] However, little is known in physically crosslinked composite gels, and the step-strain, as a non-equilibrium test, could possibly introduce hardening or thinning effects. We always conduct step-strain as the final test and terminate the simulation after it, since it might destroy the static structure of network. These two tests, in our research, gave qualitatively consistent trends.

Percolation of polymer networks is closely related to the gelation transition. We determine a polymer is bonded to a platelet filler if the distance between the end-monomer and any spheres of the filler is smaller than 1.12σ, and define a connected cluster as percolating if a continuous path, along the connected cluster, exist between each pair of opposite boundaries. The fraction of percolated polymers is calculated as a time averaged manner: snapshots (particle coordinates) are recorded every 50τ, the fraction of percolated polymers is calculated for each snapshot and averaged over 200 continuous samples. All results on structures are post time-averaged in a similar way for at least a hundred samples. Many other tests are also employed, the details of which would be introduced when we discuss the results.

3.3 Results and Discussions

3.3.1 Percolating Polymer Network

As we turn on physical bonding by setting ε_b equals to 5, a net-attraction force is present between end-monomer and nanoplatelet fillers, and the end-monomers start to physically bond to platelets. Some polymers connected neighbor platelets by having end monomers bonded to both platelets. The polymers therefore form clusters that grow with more platelets added, and gradually percolate the simulation domain. We observed a percolating network starts to appear at a platelet fraction as low as 0.29%, shown in Figure 4a, this kind of percolating network is however transient since the physical bond is reversible. Plotting only the connecting chains, as in Figure 4b, reveals this network is weakly connected: nanoplatelets are mostly separated at a large distance at this low filler concentration and only a few extended polymers are able to connect platelet fillers. The network thus has small connectivity and easily separates into non-percolating clusters if any of the physical bonds between polymer and platelet are broken up. At higher fraction of platelet fillers, the distance between plates decreased and more polymers were connecting platelets, as shown in Figure 2. Percolated network with large connectivity formed at this platelet fraction of 1.16%. The crosslinking density was so high that the breaking of any single physical bond has limited effects on the overall network. Numerical tests also proved this network persistently percolates during the simulation even though the physical bonds are dynamically forming and breaking.

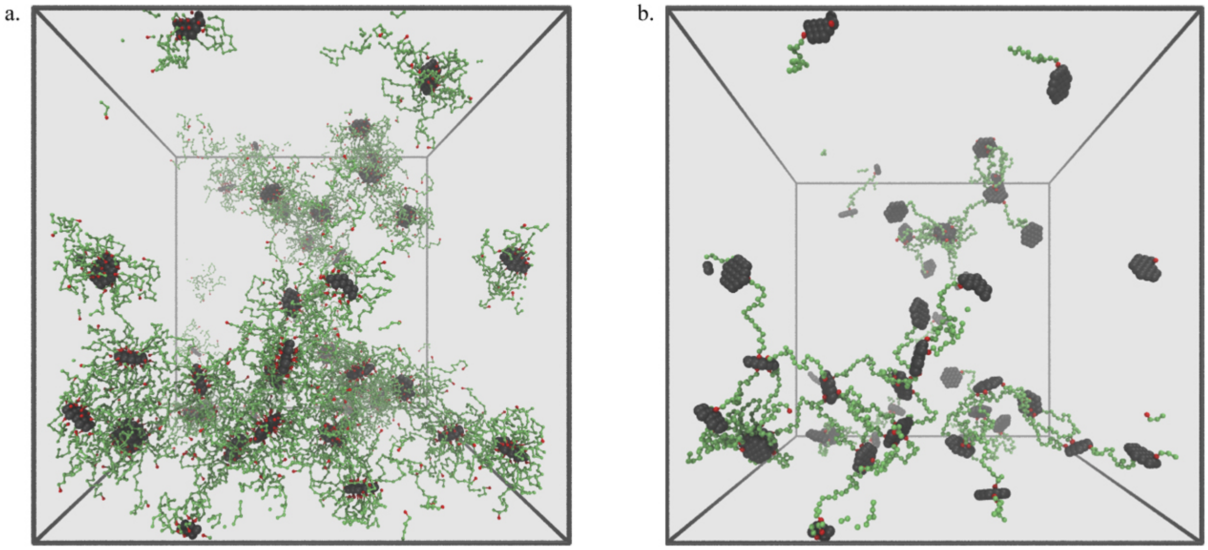

Figure 4. Percolated polymer network observed at 0.29*vol*% nanoplatelet fillers. (a). All polymers and fillers belong to the network. (b). Only the polymers that connecting platelets are depicted. In the figure, black spheres are nanoplatelets, red spheres are the end-monomers and green spheres are other polymers.

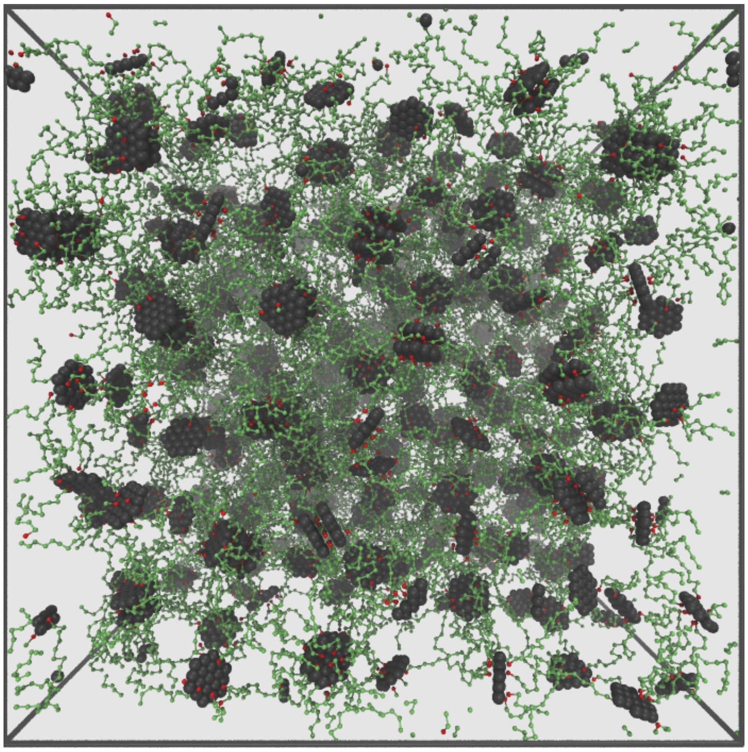

Figure 5. Percolated polymer network at 1.16*vol*% nanoplatelet fillers. Only the polymers that connect platelets are shown in the figure, black spheres are nanoplatelets, red spheres are the end monomers and green spheres are other polymers.

The sol-gel fraction was calculated and is shown in Figure 6, by considering percolated networks as the gel phase. The presented result reflects the time-averaged value of the gel fractions, for which the transient percolation networks have limited effects on the value of gel fraction presented. The time averaged gel fraction is almost 0 with 0.29% fractions of platelet filler, even though percolating network has been observed at this filler concentration. The gel phase fraction dramatically increases when platelet increased from 0.29% to 1.16%. The turning point of the increasing rate indicates percolating transition at about 0.87% platelets, at which volume fraction 84% of polymers are in the percolated network. Numerical tests show the gel phase is mainly a single large network while the sol phase consists of free polymer chains.

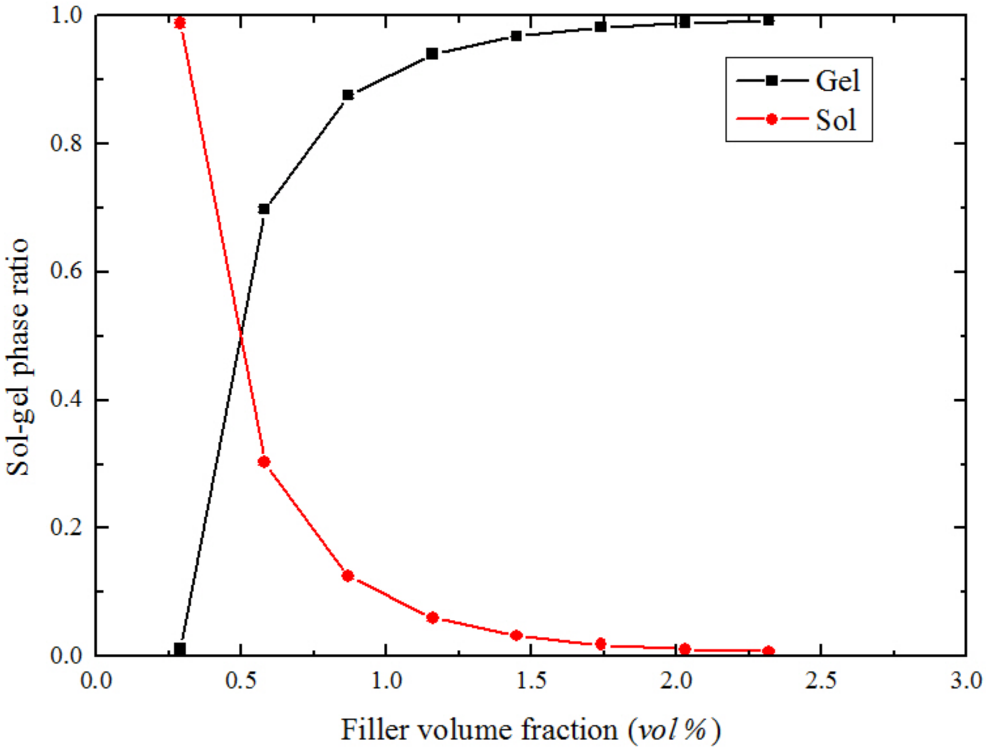

Figure 6. Solution phase and gel phase fraction at different nanoplatelet filler concentrations.

3.3.2 Polymer Dynamics

Polymers have distinct patterns of motion at different platelets fractions, as shown by mean square displacement curves in Figure 7. Polymer motion is identical in the ballistic region where the diffusion time is smaller than 10τ. In this region, particles fluctuate about their original positions with small displacements. Significant differences start to appear in the intermediate time range, with the curves apparently flattening with increased filler fraction, This behavior is a result of polymers being dynamically arrested when they are physically bonded to platelets. With a closer look at Figure 7, by increasing nanoplatelet loading, the duration of the flattened region extended longer as well as the displacement of region become smaller. The mechanism might be that platelets formed "cages" to stabilize polymers and the cages become smaller as the platelet density increases, which results in a longer time for polymers to escape from a tighter cage.[110] At longer time, polymers show diffusive behavior since the time scale is larger than the effective time of caging. In all the curves, the intermediate caging occurred at a displacement distance about 10σ, much higher than typical glass forming region, about 0.1σ.[96] It is evidence that the changes in polymer dynamics are mostly due to polymer-platelet interactions and the organic-inorganic network structure.

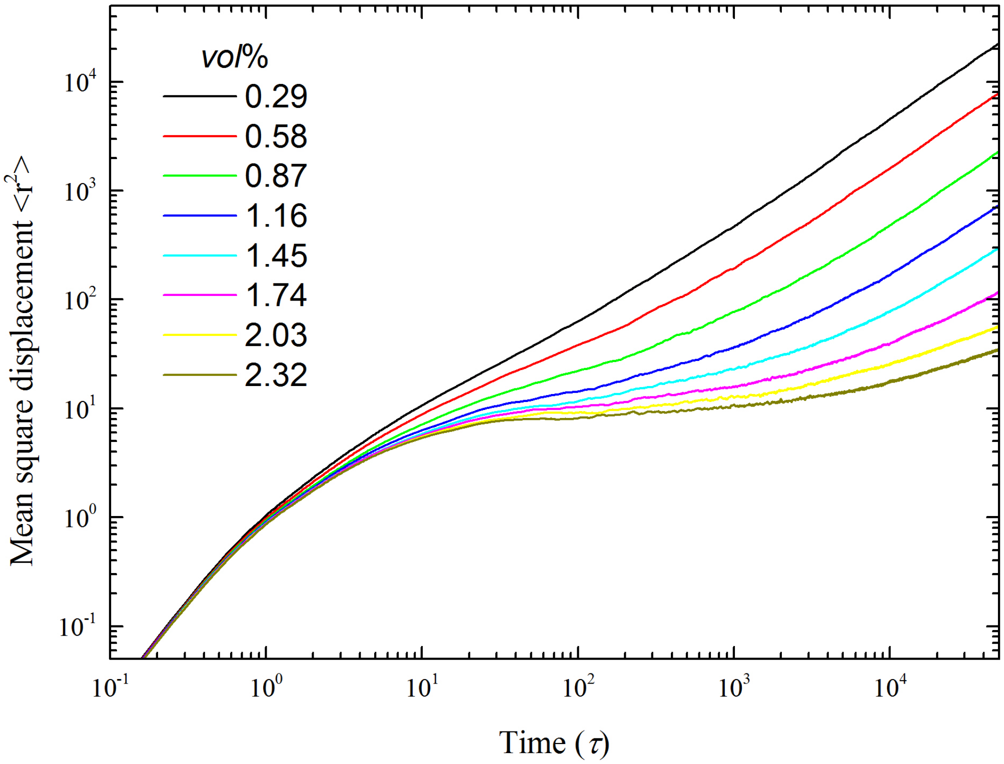

Figure 7. Mean square displacements of polymers as a function of diffusion time. The platelets volume fraction is 0.29%, 0.58%, 0.87%, 1.16%, 1.45%, 1.74%, 2.03%, and 2.32% for the curves from top to bottom respectively.

The mean square displacement, as a collective property, neglects the fact that each polymer chain has distinct states in gel systems. In our composite system, the polymers can be classified into three types: the free chains that not connected to any platelets; the dangling chains that have only one end bonded to platelets or have both ends bonded to the same platelet; and the bridges chains that have two ends bonded to distinct platelets and act as connecting agent. As shown in Figure 8, at low platelet fraction 0.29*vol*%, majority of the chains are at free state while another big portion are dangling chains. As the platelets loading increase, the free chains decreased dramatically, the dangling chains initially increased due to more chance to bond to platelets but decrease at higher platelet fraction as a result of transformed into bridge chains. And most importantly, the bridge chains steady increase with higher platelet loading, which is a direct proof of increased crosslinking density and consistent with classical network theories.

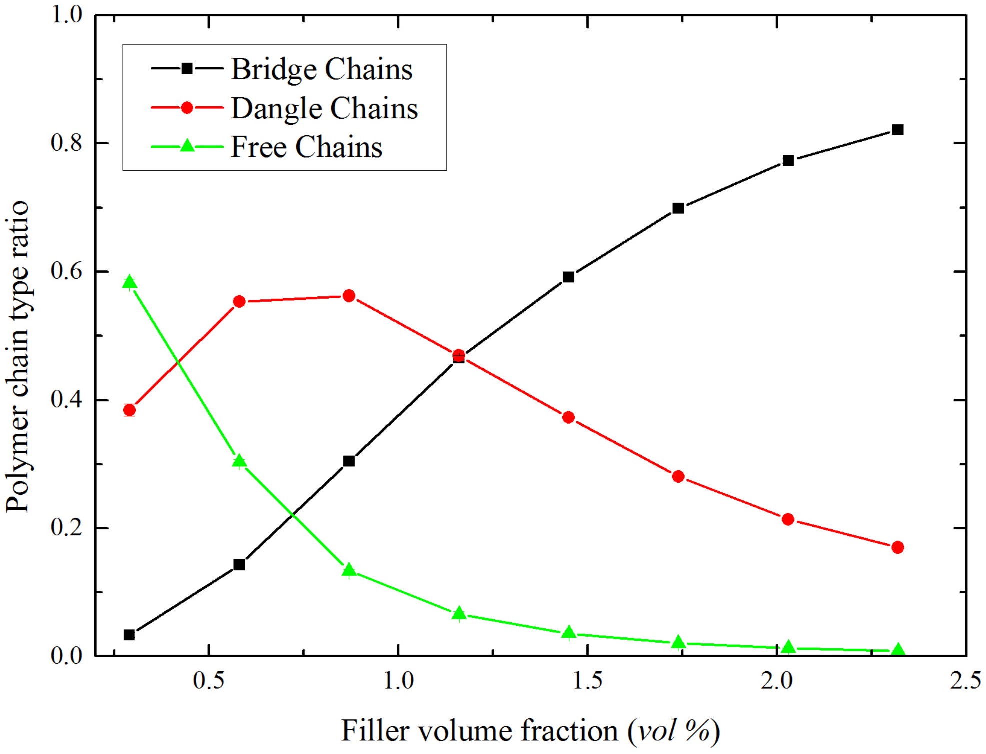

Figure 8. Three types of polymers chains, bridge chains (black squares), dangling chains (red circles) and free chains (green triangles), at different nanoplatelet filler concentrations.

In each of these states, we can characterize the internal dynamics of the polymer by defining a non-Gaussian parameter α,[111]

$$\alpha(t) = \frac{3\langle r^4(t)\rangle}{5\langle r^2(t)\rangle^2} - 1 \tag{21}$$

r(*t*) is the displacement of polymers in time span *t,* and the bracket indicate time average over all polymers. The non-Gaussian parameter α equals 0 for homogenous movements (purely random), and increase with the heterogeneity of motion. Figure 9 shows a significant peak appears with increased platelet fractions, indicating very strong heterogeneous behavior. This can be explained by the 3 different types of polymer chains as in Figure 8. The free chains have comparatively smallest spatial constraint and therefore move much faster. In contrast, the dangling chains move slower since they are tethered by platelets, and bridge chains experience mostly collective motions with the clusters they belong to. The peak value, as in Figure 6, initially climbs with filler fraction but is lowered when filler fraction increased from 0.87% to 1.16%, coinciding with the percolation transition and indicating the collective motion of the percolated network becomes significant. The non-Gaussian curve also complements the mean-square displacement curve by indicating more clearly the duration of the caging. The non-Gaussian parameter decays at long times in the diffusive region, but clearly the system with high platelet fraction, for example 2.32%, still retains large non-Gaussian parameter value even at $5\times10^4\tau$, indicating this time is still within the range of caging for those systems.

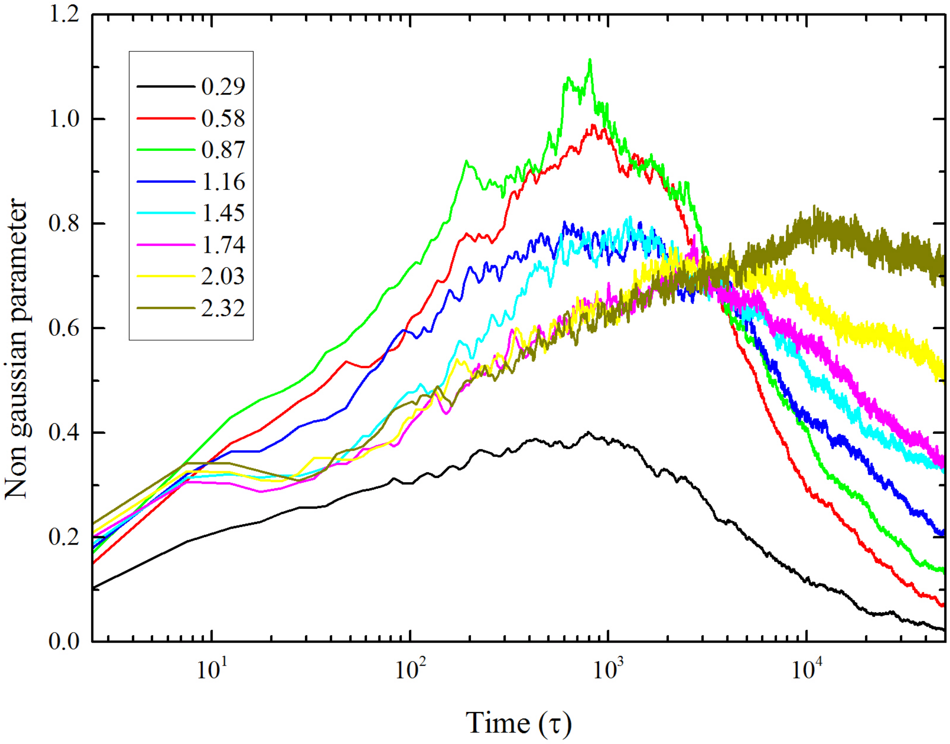

Figure 9. Non-Gaussian parameter of polymers at different diffusion time of composite systems at filler concentration 0.29%, 0.58%, 0.87%, 1.16%, 1.45%, 1.74%, 2.03%, and 2.32%.

3.3.3 Gel Mechanics

The significant changes in mechanical properties are the most direct measure of gelation. We measured the mechanics both by stress auto-correlation and stress relaxation. In Figure 10, the semi-log value of stress auto-correlation function is plotted for various platelet filler fractions. The plateau value at higher platelets loading is consistently larger than those with lower platelet fractions, except at a few points due to the fluctuation. For platelet fraction in the range of 0.29% to 1.16%, the values all decay to zero within the longest correlation time that we measured. An apparent non-zero tail remains for systems with higher filler fraction, more clearly seen from the inset of Figure 10, in which tail part of the curve is enlarged and plotted linearly against correlation time. The Green-Kubo integration would obviously result in discontinuous increase in the shear viscosity when filler fraction increased from 1.16% to 1.45%. This clearly indicates the viscosity was described by two different mechanisms at low and high platelet loadings with the transition at about 1.16%. At even higher platelet fraction, the decay of stress auto-correlation function is extremely slow, indicating much higher viscosity, and a transition to a solid-like state.

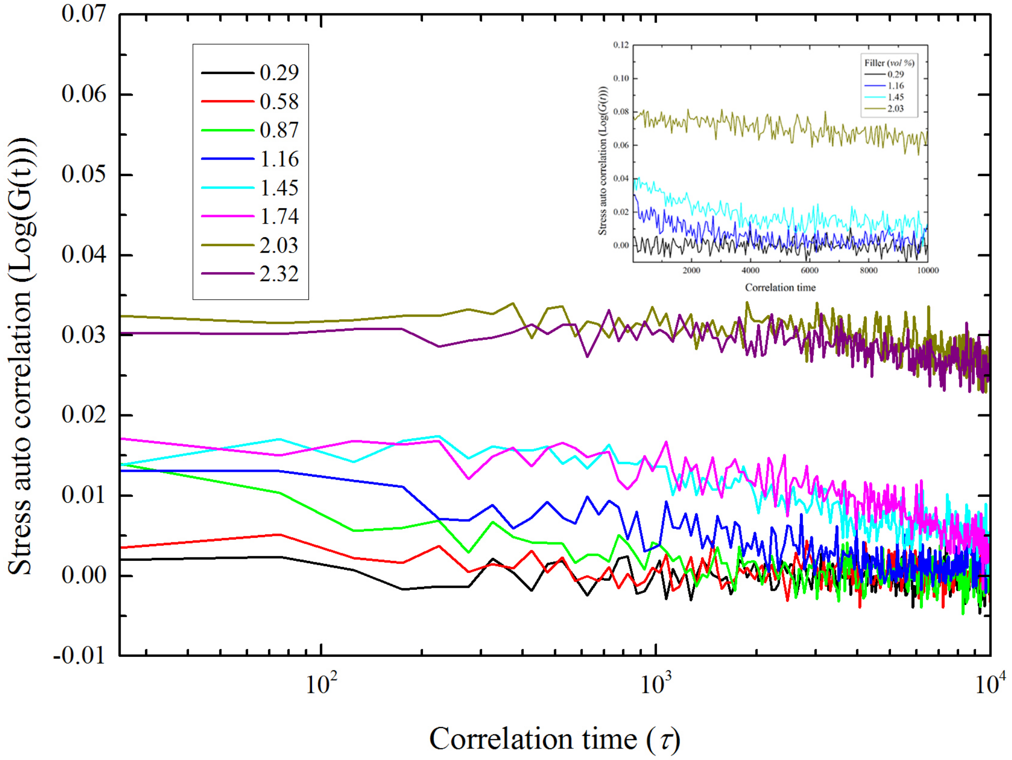

Figure 10. The semi-log value of stress auto-correlation function G(t) at different platelet fractions. The inset picture shows the tail value of SAC as a linear function to time for selected filler concentrations.

The relaxation of normal stress after elongating the simulation domain by 100% shows similar trends of mechanical behavior as those in the stress auto-correlation test. As in Figure 11, the normal tension consistently increased with filler fraction after we strained the simulated composites, which indicates the elastic energy of the composites increased as more platelets were added into it. In a composite with more than 1.45*vol*% fillers, a non-zero tail remains in stress relaxation curve until $2.5\times10^4\tau$, the end of the time we calculated the normal tension, indicating a much larger elastic energy than those composites with lower filler concentration. This is further evidence that composites have become "solid-like" at this nanoplatelet filler loading. The two mechanical tests prove our simulated composites have changed mechanically from solution state to gel state by adding more platelet fillers, however, the mechanical transition point is slightly larger than that of the percolation transition.

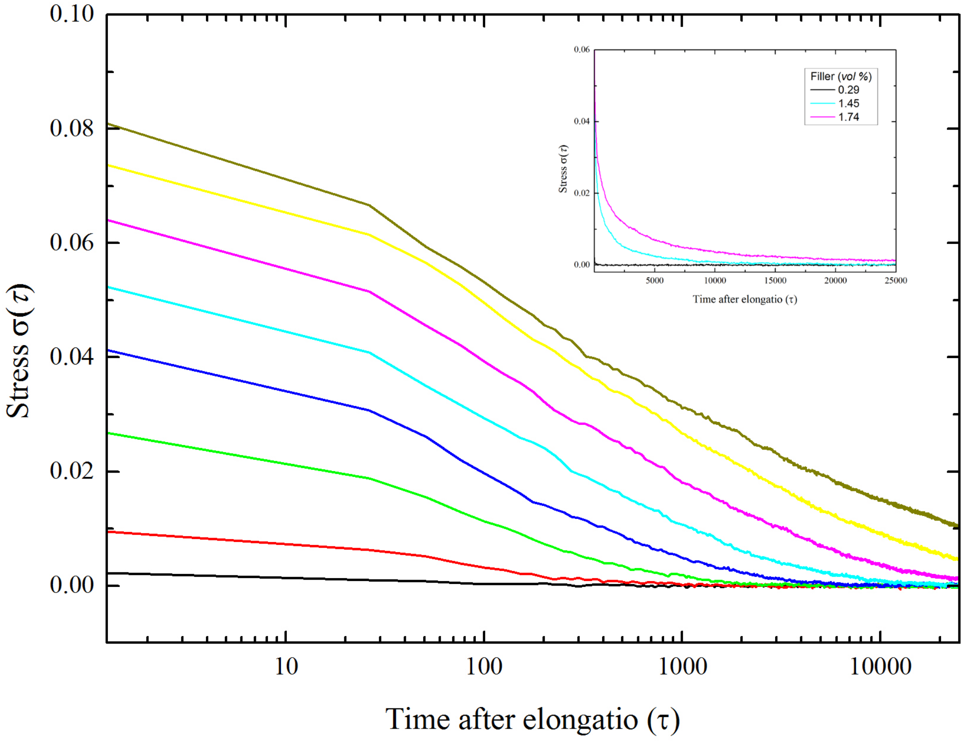

Figure 11. Normal tensions of composites at different time after elongating the simulation domain by 100%. The platelets volume fraction is 0.29%, 0.58%, 0.87%, 1.16%, 1.45%, 1.74%, 2.03%, and 2.32% from top to bottom respectively.

3.3.4 Structure of Nanoplatelet Fillers

From earlier studies of platelet colloids,[39-40,100] we know that platelets could organize into different structures, exfoliated states, stacked states, and intercalated states. We observed platelets formed an intercalation structure in our simulated composite gels that made them very unique compare to those with sphere fillers. As seen from the Figure 12a and b, the end-monomers, which are represented by the red spheres, densely wrap around both type of fillers, these end-monomers introduced indirect attractions between neighboring fillers, which cause fillers to aggregate into small groups. However, the sphere filler aggregated into non-ordered bulk phases, while nanoplatelet fillers formed layered intercalation structures due to the anisotropic nature of the filler. The polymers surround these intercalated platelets also helps to stabilize these intercalation structure and prevent them from further aggregation. These intercalated structures as connected by polymers play the role as the crosslinking nodes of the organic-inorganic networks, and is the most unique structural character that distinguish nanoplatelets filled gels from nanosphere filled gels.

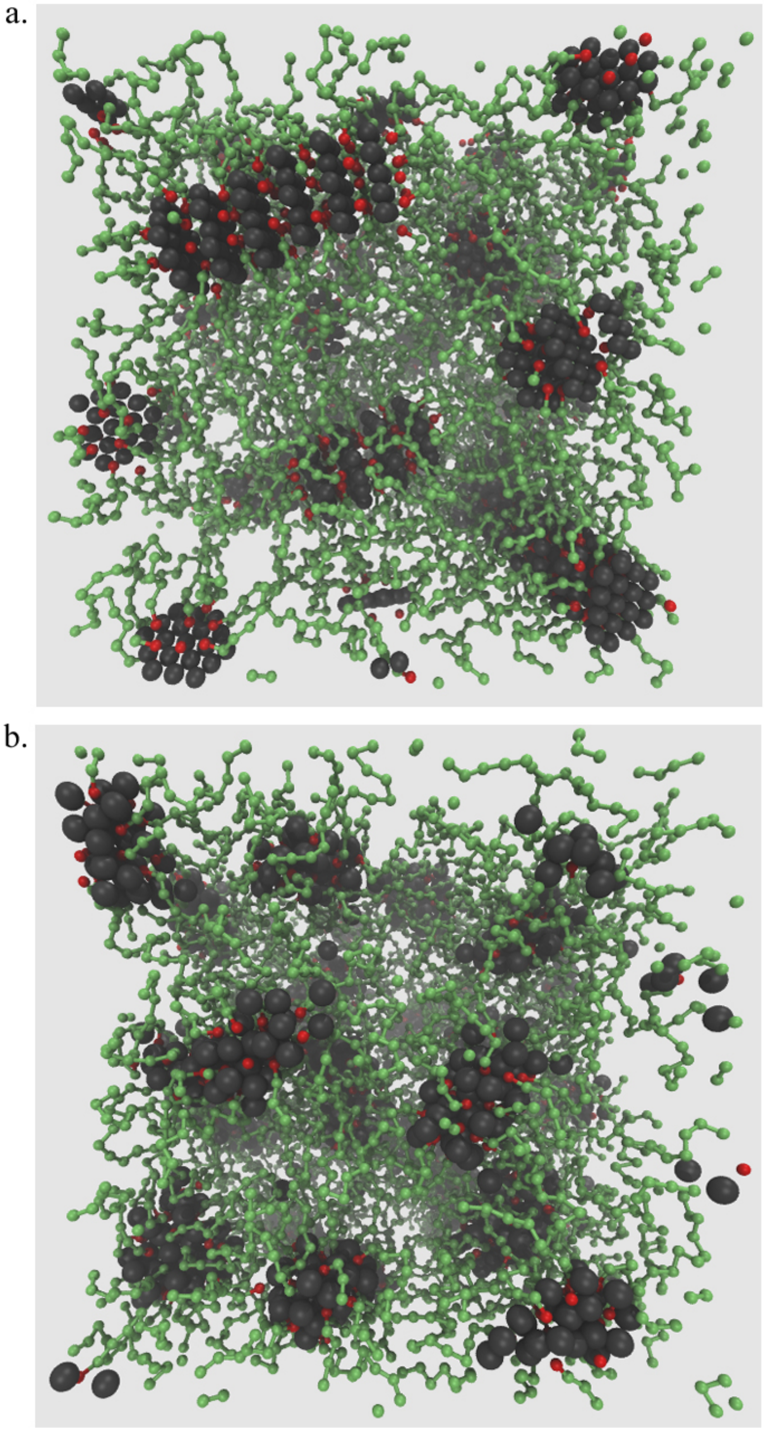

Figure 12. (a) The network structure of platelet filler and polymer composites. (b) The network structure of sphere filler and polymer composites. Both systems are at filler fraction 2.03*vol%* and with same simulation parameters. The picture represents enlarged partial view of the overall composites.

The physical bonding between end-monomers and fillers can be characterized by radial distribution function and compared between spherical fillers and platelet fillers. In Figure 13, the radial distribution functions shows a strong peak at a distance of 1.12σ both for platelet filler and sphere fillers, this is the evidence of physical bonding that cause end monomers to localize at fillers' surface. The function flattened at larger distance for sphere fillers while second and third peak arise at the same region for platelets fillers. The radial distribution function also shows no significant difference when the filler concentration increased from 0.29% to 2.03% indicating the local bonding is not affected by percolation transition. The radial distribution function of platelets to platelets is also measured by using center-to-center distance. As shown in Figure 14, no neighboring platelets were found until a large peak appears at distance about 1.9σ, then dropped rapidly to zero until another peak appears at distance about 3.8σ. The two peaks indicating neighboring platelets are exclusively located at these two distances; the distance of the first peak, 1.9σ, exactly match an intercalation structure with one layer of polymers sandwiched between two platelets, and the second peak is a result of two platelet that separated by another layer of platelets within the same intercalation group. Similar to that of Figure 13, the intercalation structure of platelets, is not affected much by percolation.

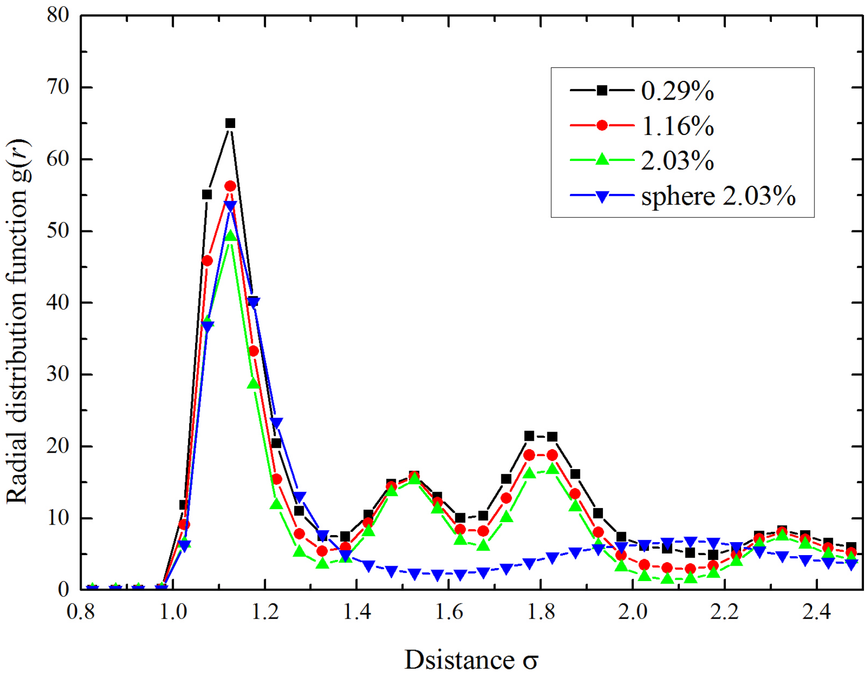

Figure 13. The radial distribution function g(*r*) of end-monomers to platelet fillers, at volume fraction 0.29%, 1.16%, 2.03%, and for sphere fillers at 2.03%. The simulation parameters are the same for sphere and platelet fillers.

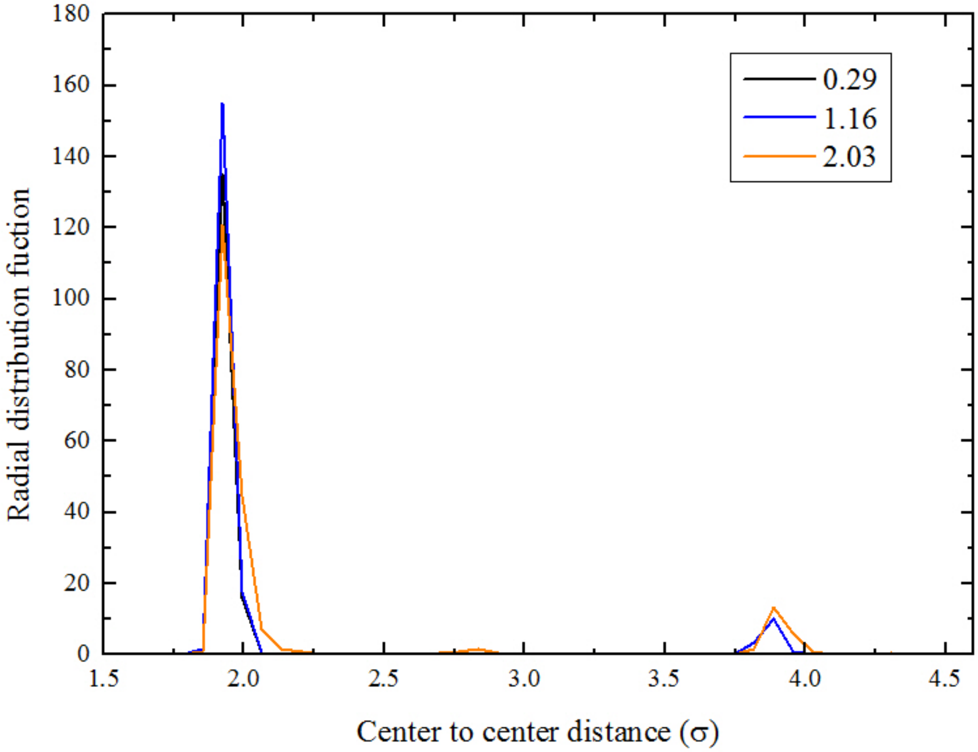

Figure 14. The radial distribution function g(*r*) of platelets to platelets measured by using the distance between the center of mass of each platelet.

The orientation ordering of platelets is characterized by using second Legendre polynomial of the form

$$P(r) = \langle \frac{1}{2}(3cos^2\theta(r) - 1)\rangle \tag{22}$$

θ(*r*) is the angle between the norms of two platelets separated at distance *r*. This polynomial P(*r*) equals to 1 for paralleled norms, equals to 0 for random ordering, and equals to -0.5 for perpendicular norms. As seen from Figure 15, at the lowest filler fraction 0.29%, the polynomial has a value close to 1 within a distance of 2.0σ but dropped to 0 at larger distance, this is due to small intercalation that has only two layers of platelets which is common at low platelet fractions. At higher platelet fraction, 1.16%, larger intercalation forms, the polynomial retains a value close to 1 until about 8.0σ, it indicates there is negligible small amount of random orientated platelets within a neighbor range of 8.0σ. The polynomial didn't extend to longer distance at higher platelet fractions, this is because the distance between distinct intercalations is getting smaller at higher platelet density, since there is no orientation correlation between two independent intercalation structures. For all curves, the polynomial finally decays to 0 at long distance showing there is no global ordering of the composite gel. The radial distribution function and second Legendre polynomial proved local intercalation structure with one layer of polymers between platelets is a highly preferred local structure for the platelets fillers.

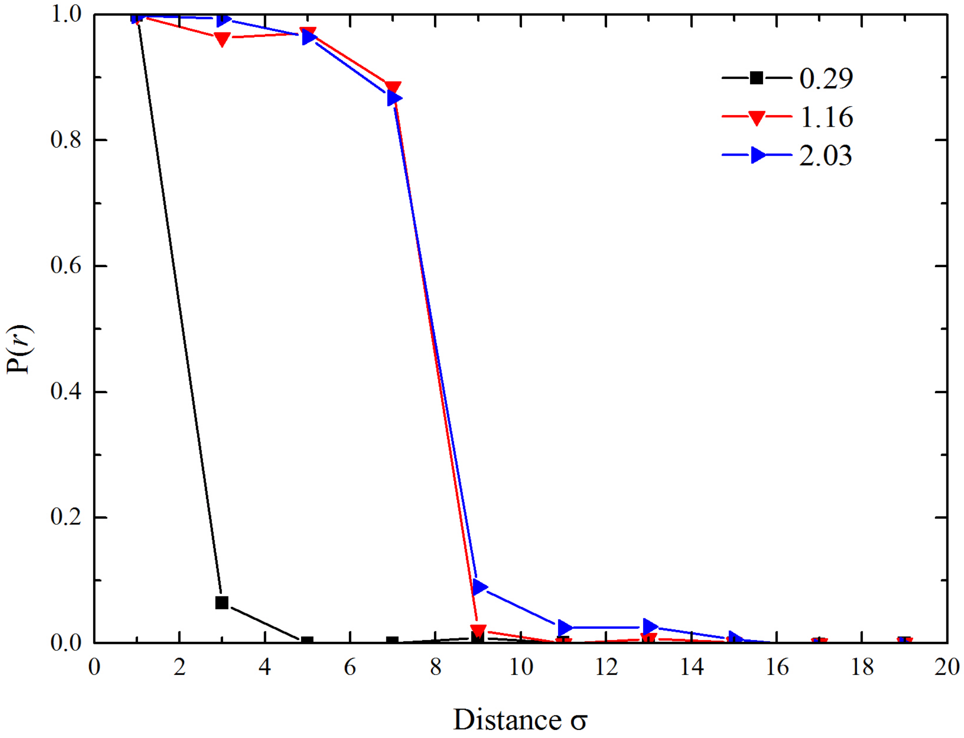

Figure 15. Second Legendre polynomial of platelet at volume fraction 0.29%, 1.16% and 2.03%.

We define two platelets to be in the same intercalation structure if their center-to-center distance is less than 2.0σ and the angle between their norms is less than 20°, the probability mass function of intercalation size could therefore be calculated, as shown in Figure 16. At the lowest platelet fraction, 0.29%, the exfoliated state dominates and the largest intercalation size is about 3 layers of platelets. As the volume fraction of platelets increase, the intercalation size also steadily increased, at 1.16*vol*%, more and larger intercalations were found compare to 0.29%. At 2.03%, a peak appears at 3 indicating majority of the intercalation structures have 3 platelets, the curve also shows exfoliated state almost disappear at this comparatively high platelet volume fraction, and heavier tail appears indicating the formation of very large intercalations. In experiment condition, the size of intercalation might be smaller, because real platelets have larger spatial constraints and opposite charges would also affect the aggregation structure.

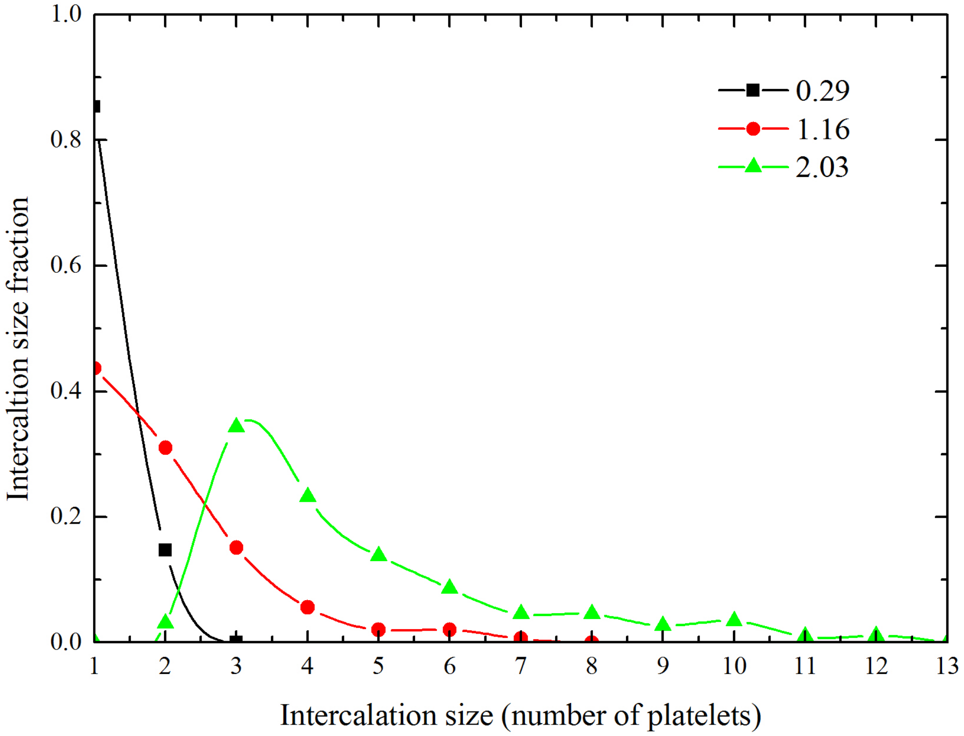

Figure 16. The probability mass function of the size of the intercalation structure at platelet volume fraction 0.29%, 1.16% and 2.03%.

We also compared the stress auto-correlation function between composites with sphere fillers and composites with platelets fillers at various filler fractions above the percolation transition. As shown in Figure 17, platelet fillers show consistently larger enhancement on the stress auto-correlation function than the sphere fillers at volume fraction 1.45% and 2.03%. It is worth to be noted, the gel fraction of the platelet filled gel is also slightly larger than that of sphere fillers, the gel fraction of sphere fillers is about 85% while the gel fraction is about 98% for platelet fillers. With all the evidence from the molecular structures, we conjecture the advantage of platelet fillers in improving the mechanics of polymer gels might comes from two parts. First, the platelets provide larger net attraction to end-monomers since multiple points of the platelets is exerting force to the polymers; the platelet also provided extended surface for bonding, which promoted crosslinking. Second, the large intercalation structures that act as crosslink nodes have huge spatial constraints; these large local structures significantly reduced the fluctuations of networks and cause the network become more affine like.

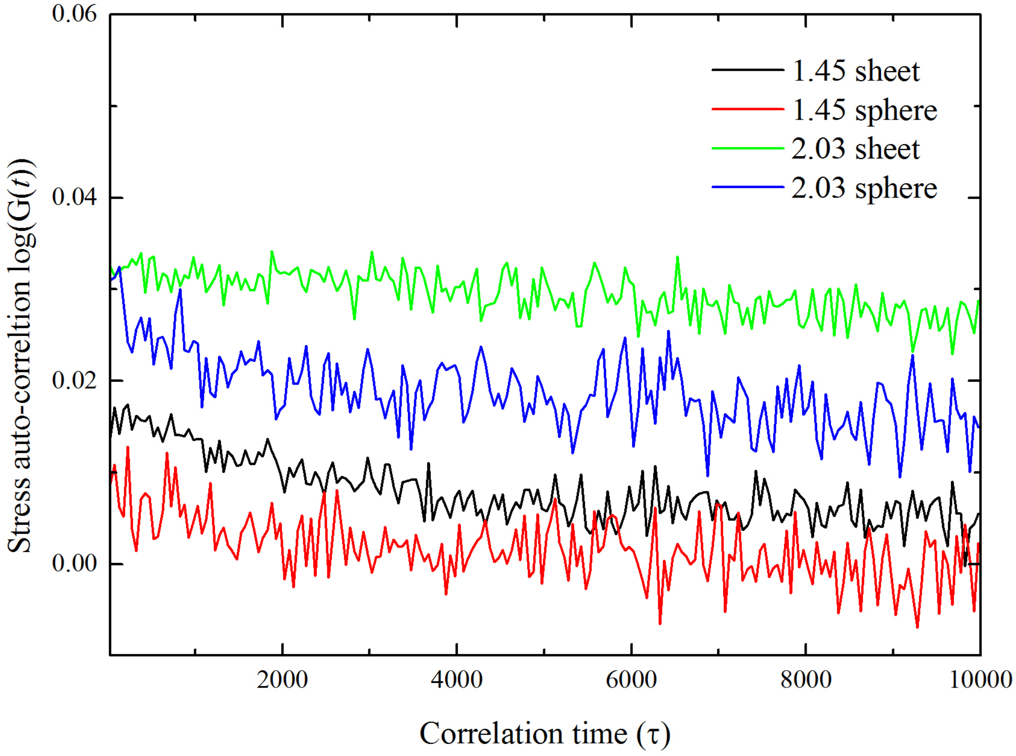

Figure 17. Stress auto-correlation function G(*t*) of composites with sphere fillers and with platelet filler at filler volume fraction 1.45%, and 2.03%. The value is calculated by equation 3, and we use semi-log transform of the form $\pm\log(1+|G(t)|)$, where the sign is same as G(*t*).

The network structure and the structure of platelet fillers are sensitive to many factors. We investigated a system with slightly different condition.[112] The polymers have length 30 and the functional monomers are distributed at every 5th of the monomers (instead of only the two ends), the system also has explicit Lennard Jones solvents with $\varepsilon = 1.0$ to all particles (good solvent condition). A very different gel network structure was observed, as in Figure 18, most of the platelet fillers have random orientation and there is no intercalation. The polymer network is also depleted from the solvents, which made the network to show “fibrous” structure. We think the major difference of the two systems is the density and distribution of the functional monomers. Even at the same polymer concentration, the density of the functional monomer differs as much as 2 times. The monomers at the same chain wraps around platelets fillers and prevents them from forming intercalations, since the monomers inside the chain are more constrained to reorder themselves as end-monomers could. The structure of the organic-inorganic network could obviously be affected by other factors such as solvent quality, it however requires more investigation case by case.

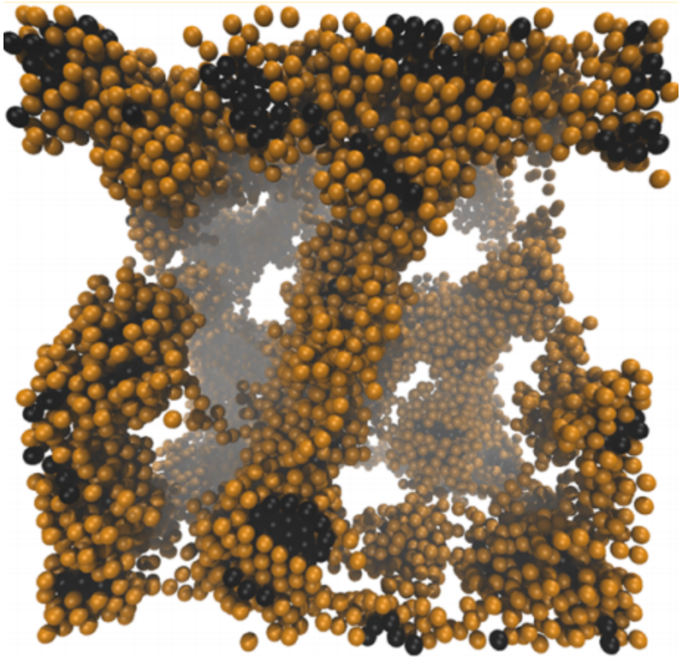

Figure 18. Network structure in simulation with explicit Lennard Jones solvents, the polymers have length 30 and the functional monomers are distributed at every 5^{th} of the monomers.

3.4 Conclusion

In conclusion, we designed a generic model to simulate polymer-platelet composite system where the gelation is by the short-range physical attraction between end-monomers and platelet fillers. We have shown large percolating networks formed as a result of polymers crosslinked by platelets. The gelation mechanism is similar to that of pure polymer gels; namely the sol-gel transition; the intermediate “caging” region of mean square displacements; and the heterogeneous movement of polymers as a result of three distinct states, dangling, free, and bridging. The mechanical tests show composites become “solid-like” gels by adding platelet fillers. The platelets aggregate into intercalation structure, in which the norms of the platelets are parallel to each other and there is one layer of polymers sandwiched between two platelets. The intercalation structure act as crosslinking node of the network and has made the composite unique compare to those with spherical fillers. The simulation results cast light on the molecular structure that forms in platelet filled polymer composites. The intercalation structure observed is helpful to investigate the reasons of the superior effect that platelet fillers has on the mechanics of composites gels. The systematic analysis of the structure and mechanics will be useful to guide designs of novel composites gels.

Chapter 4. Nanofillers as Interfacial Compatibilizer

4.1 Introduction

Polymer blends, which consist of two or more different polymers, have been widely investigated, since they offer the possibility of combining the properties from different polymers into a single material.[113] For instance, in theory it should be possible to improve the strength of the material (relative to a homopolymer) and to produce blends with unique optical, thermal properties, or special features such as biodegradablility.[114-117] It is generally considered as very economic way to enhance the properties of materials by combining the desirable characteristics of two components.

Polymer blends, however, are difficult to make since most polymers are chemically immiscible. This has lead to many problems of polymer blends, such as thermally instability, microstate phase segregation and mechanical weakness.[113,118-119] It is therefore critical to control the phase behavior of polymer blend in order to get useful polymer products. Introducing a third component into polymer blends is a common scheme to increase interfacial compatibility of the two polymers. The kinds of components include but are not limited to surfactants, diblock copolymers, triblock copolymers and nanofillers.[120-121] In recent years, anisotropic fillers, such as carbon nanotubes and layered silicate fillers have also been applied to polymer blends.[120,122-125] For example, inter-layer distances of clay fillers were found to have great impact on thermal and rheology properties of PC/PMMA blends.[114,123]

Although the miscibility of two polymers is not the main point of interest in this work (we used exclusively immiscible polymers in this chapter), an understanding of mixing behavior from a thermodynamic aspect is useful to understand the results and to design experiments. For two polymer to be miscible, it's necessary that the free energy of mixing $\Delta G_{mix} < 0$, Based on the Flory Huggins theory, the free energy of mixing can be written as:

$$\Delta G_{mix} = \frac{RTV}{V_r}\left[\left(\frac{\phi_A}{x_A}\right) ln\phi_A + \left(\frac{\phi_B}{x_B}\right) ln\phi_B + \chi_{AB}\phi_A\phi_B\right] \tag{23}$$

Here , Vr is the volume of repeating units, ϕ_A and ϕ_B are the volume fractions of the two polymer, x_A and x_B are the molecular weights of the two polymers, χ_{AB} is the Flory interaction parameter. The critical condition of phase separation can then be calculated as:

$$\chi_{AB}^{*} = \frac{1}{2}\left[\frac{1}{x_A^{1/2}} + \frac{1}{x_B^{1/2}}\right]^2 \tag{24}$$

$$\phi_A^{*} = \frac{x_B^{1/2}}{x_A^{1/2}+x_B^{1/2}} \tag{25}$$

$$\phi_B^{*} = \frac{x_A^{1/2}}{x_A^{1/2}+x_B^{1/2}} \tag{26}$$

Earlier studies have shown that the Flory-Huggins interaction parameter can be linked to the commonly used simulation parameter ε, and this can also be applied to our simulation.[126] Another important point is how to measure the strength of the interface. Interfacial slip is a phenomenon when at a shear stress σ, that is greater than a critical value, slippage occurs at the interface, in other words a non-zero velocity is observed at the interface under shearing.[127-128] This kind of slippage is not limited to polymer-polymer interfaces but also can be applied to interfaces such as polymer/solid interfaces. Many studies have focused on understanding the mechanism and connection between interfacial structures, viscosity and slippage.[129-131]

In this chapter, we utilize molecular dynamic simulation to study the interfacial behavior of binary polymer mixture. Our purpose of study is to unveil the function of nanofiller on the properties of polymer blends, specifically the interfacial tension and interfacial slippage. The factors we studied include the structure (type) of fillers, filler loadings and affinity of filler to polymers. We thoroughly investigated the structures and dynamics at the interfaces of such system, and analyzed the structure-property relationships. The type of fillers we studied includes spherical fillers, anisotropic filler of sheet shape or tube shape and diblock copolymer fillers. We studied the simulated system both in static and non-equilibrium (shearing) condition. We studied the mechanism of nanofiller on reducing polymer-polymer interfacial energy and interfacial slippage. We proved the mechanism and degree of improvement intrinsically differed between different types of fillers.

4.2 Model and Methods

4.2.1 Simulation Model

As shown in Figure 19, the initial simulation domain is a cubic box of length 40 σ; 400 polymer A chains and 400 polymer B chains were initialized randomly at the bottom and the top half of the simulation box respectively. Polymers are made of mono-dispersed chains consisting of 64 repeating segments. This length is a bit longer than the entanglement threshold calculated by Kremer and Grest, which they believe is about 35 repeating segments.[58-59] This initial configuration was chosen so that a planar single interface between the two polymers is generated. Preliminary simulations have shown that mixed immiscible polymers would also lead to layered phase separation very close to this one, but at extraordinary long simulation time.

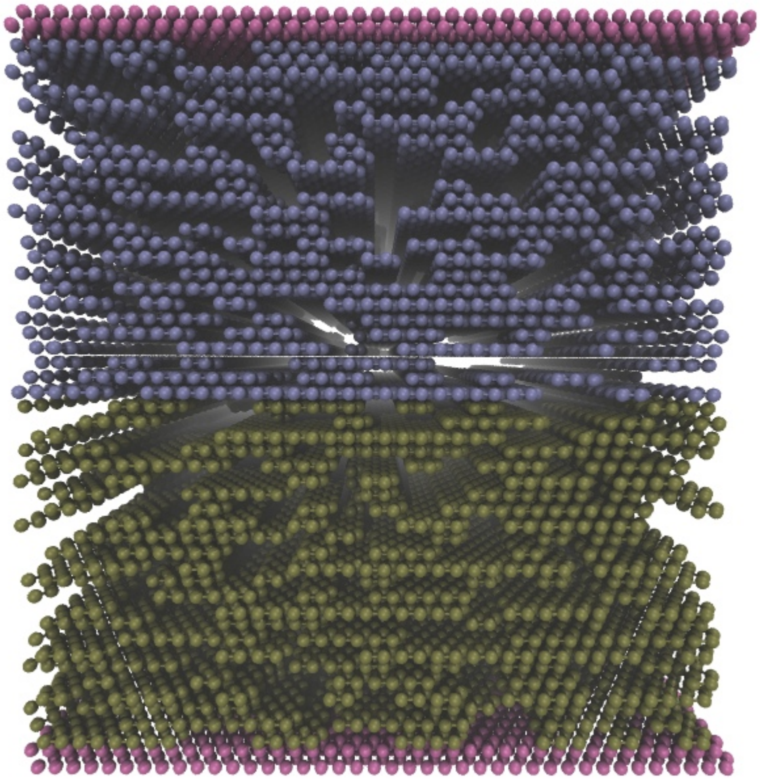

Figure 19. The Initial configuration of simulated polymer blend system. Top and bottom of the simulation box is confined to two layers of walls (pink layers). Polymer A (bottom half) and Polymer B (top half) are randomly arranged in fcc(111) lattice to form a bilayer structure.

The simulation domain is bounded by two walls at top and bottom. Each wall consists of two layers of unit sized LJ spheres in a densely packed hexagon lattice. The wall remains static at all time, and serves two functions in our simulation. Firstly, instead of using Nose-Hoover style barostat, we applied constant force on the top wall at direction to the bottom (-z) while keep the bottom wall fixed at z direction. The relation between applied forces on each wall particles and pressure has the simple form:

$$f = \frac{P * S_{wall}}{N_{wall}} \tag{17}$$

in , f is the force applied to each particle of the top wall, P is the target pressure, and S_{wall} is the area of the wall, which is simply $1600\sigma^2$, and N_{wall} is the number of wall particles. We also limited the movement of top wall to be less than 0.001σ at each simulation step to avoid wild oscillations. Secondly, the wall is how we applied real shearing to the simulated blends. Initially, both walls were kept fixed at x and y direction. After equilibrium, we toggle shearing at constant speed by moving top and bottom wall at specified speed in opposite directions ($+x$ and $-x$). In this way, a velocity profile is imposed on the polymer blend system.

4.2.2 Model Parameters

We employed a MD model that is similar to the KG model introduced in Chapter 2. For all the simulations in this chapter, two types of polymers are mixed in the melt state, with fillers at different concentration and of different types. All polymers and fillers are coupled to a background heat bath at a temperature 1.1ε by Nose-Hoover thermostat. It is worth to note this temperature is above the glass transition temperature of the simulated KG polymers. Particle trajectories are integrated by Verlet-velocity method at step size 0.005τ.

We used potential fields exactly the same as what we have in previous hydrogels chapter and described in Chapter 2. Lennard Jones potential in Equation 14 is applied to all pairwise particle interactions; polymer chains were bonded by FENE potential, Equation 15, with all the parameter same as KG model. We however used modified LJ potential for spherical fillers that is not unit sized:

$$V^{LJ}(r) = \begin{cases} 4\varepsilon\left[\left(\frac{\sigma}{r-\Delta}\right)^{12} - \left(\frac{\sigma}{r-\Delta}\right)^{6}\right], & r \le r_c + \Delta \\ 0, & r \ge r_c + \Delta \end{cases} \tag{28}$$

This equation is the same as the classical LJ equation except that distance is shifted by Δ which accounts for the additional size of the filler, in our simulation we set Δ=0.5 for spherical fillers equals to a fixed diameter of 2.0σ. Our study investigates not only type of fillers but also the miscibility between two polymers and adhesion of filler to polymer matrix, both controlled by ε_{ab} *and* $\varepsilon_{\mathrm{fp}}$ respectively. Large value of ε=4.0 was applied to polymer and wall interactions to ensure no slips at the wall.

4.2.3 Nanofillers

We investigated four types of fillers. As shown in Figure 20a, we investigated finite sized spherical filler with diameter 2.0σ, twice the size of other particles. We investigated diblock copolymer with 64 segments, same length as the polymer matrix, half of the diblock is made of A type, which is more attractive to polymer A, the other half is made of B type, which is more attractive to polymer B (Figure 20b). We also investigated platelet fillers consists of 19 unit spheres in a hexagon shape (Figure 20c) and fibrous filler with length 12.0σ and width 1.86σ (two layers of unit spheres, Figure 20d). The diblock copolymer has the same flexibility as the polymers, while platelet fillers and fibrous fillers are treated as rigid body with conserved shape during simulation.

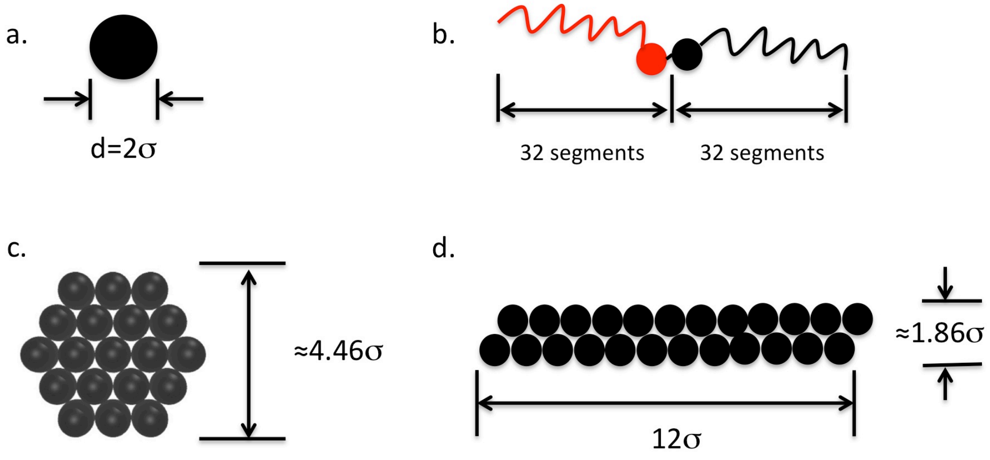

Figure 20. (a) Spherical filler with diameter 2.0σ. (b) Diblock copolymer with 64 segments, half of it is A type (attractive to polymer A), the other half is B type (attractive to polymer B). (c) Platelet filler. (d) Fibrous filler of length 1.86 σ.

To compare the effects of different fillers on tuning the interfacial property of binary polymer mixture, the concentration of fillers have to be kept constant. However, this is not applicable in a NPT ensemble since the size of the system changes in isothermal-isobaric ensemble. The density of such system is not only depended on the composition but also depended on the nature of the materials. We therefore introduce an invariant parameter, the volume ratio of fillers. The volume ratio of filler is defined as follows. System volume is defined as the total volume of particles and we used a fixed number of polymers, 400 polymer A and 400 polymer B, both with universal length of 64 beads. Volume of each Lennard-Jones sphere is simply $\frac{4}{3}\pi(\frac{\sigma}{2})^3$, which is approximately $0.524\sigma^3$. Volumes of all other species are calculated by treating Lennard-Jones sphere as the bases. Spherical fillers with diameter of 2.0σ have unit volume $4.188\sigma^3$; di-block fillers with 64 beads have unit volume of $33.510\sigma^3$; Tube fillers with 24 spheres patterned in a line segment have unit volume of $12.566\sigma^3$. For the platelet filler, the volume of the hexagon (area multiply by unit thickness) was used as the unit volume, which is $17.258\sigma^3$ for platelet of 19 spheres.

Our research focus on immiscible polymer blends, as indicated in chapter 4.1, the miscibility of polymers can theoretically be described by Flory-Huggins parameter. We noted that there are many studies that connect the Flory-Huggins parameter χ to the simulation parameter ε in either MD or MC simulations. For example, as Chremos and Nikoubashman investigated in a MC simulation of block copolymer, they were able to fit χ as a simple linear relation to temperature at fixed ε.[126] The scaling quantities are not comparable to what we have in our MD simulation, but the general trends that miscibility can be controlled by ε is consistent and was proved by our simulation results. Generally speaking, in simulated polymer blend systems, the larger ε_{ab} (between two polymer) the greater miscibility of two polymers while other system setting are kept constant.

4.2.4 Interface analysis

As indicated previously, we introduced a velocity profile across the *z* direction by applying constant shearing to top and bottom wall respectively, as shown in Figure 19. The top wall was moved at constant speed v_x to the positive *x* direction, while bottom walls were moved at same speed but in the opposite x direction. The system was divided into layers across the z direction, and the average speed of particles in each layered bin was measured as a time average over a typical time span of 5 millions simulation steps after reaching equilibrium. A homogeneous system has uniformly distributed velocity profile, so that the first derivative of *dv/dz* is continuous at all layers. This however hardly appears in an immiscible polymer blends system, for which the interface is weakly adhesive. As illustrated in Figure 21, a discontinuous velocity profile would occur in such systems beyond critical shearing speed.

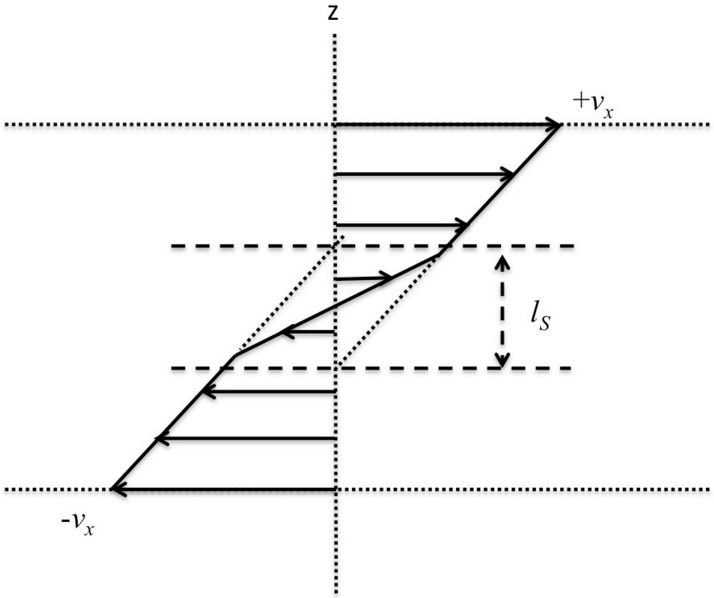

Figure 21. Illustration of interfacial slippage under constant shearing. Solid arrows indicates the direction and magnitude of velocity at discrete layers across z direction. l_S is the length between extrapolated velocity line that measures the magnitude of interfacial slippage.

Different definitions may be found in literatures regarding the interfacial slip of polymer blends. According to the definition used by de Gennes and et al.,[127] by extrapolating the velocity profile to intersect with the vertical line where velocity is 0, the slip length is the vertical length from the transition point to the intersection. As in Figure 21, we define the vertical distance l_S between two extrapolated velocity lines as the interfacial slip length. In the simulation, velocities at different *z* coordinates are calculated by dividing simulation domains into layered bins of the same thickness. We also want to note, large adhesion is applied between walls and polymers during shearing, this resulted in some oscillations in layers close to either top or bottom walls. These layers were removed in most of the calculations, not only for slip length measurements, but also for the rest of analysis. This should however not affect the correctness of our simulation, since only a small portion of layers is removed, and it's the mid region that really affects all the analysis.

A different angle to look at interfacial compatibility is to calculate the interfacial tension from thermodynamic point of view. Given the importance of interfacial energy in theoretical analysis, we employed calculation method similar to Nijmeijer et al..[132-133] The tension of planar interface is calculated by integral of the difference between normal and tangential pressure tensor over z direction from bottom to top boundary,

$$\gamma = \int_{z_{low}}^{z_{high}} [P_N(z) - P_T(z)] d_z \tag{29}$$

in the equation, $P_N(z)$ is the normal pressure component at given z coordinates layer and $P_T(z)$ is the tangential pressure component. To generalize it for our simulated system, it can be calculated in a discrete way by summation of layered pressure difference,

$$\gamma = \sum_{k=1}^{N} \gamma(k) \tag{30}$$

$$\gamma(k) = -\frac{L_z}{N_b} \langle \left\{ \sigma_{zz}(k) - \frac{1}{2}\left[\sigma_{xx}(k) + \sigma_{yy}(k)\right] \right\} \rangle \tag{31}$$

Here, the simulated system is divided into N bins of equal size across z direction, $\gamma(k)$ is the pressure difference of k_{th} bin; L_z is the total length of z direction, N_b is the number of layered bins, σ_{ee} is the per-atom stress tensor at direction ee. We refer to official LAMMPS documentary of “compute stress/atom” for the details about per-atom stress tensor calculation. Reported interfacial tension value were time-averaged results of 5,000 samples over timespan of 5 million steps.

4.3 Results

Our simulation starts from a binary mixture of two polymers with a planar interface. We control the degree of compatibility at the planar interface by varying ε_{ab} between two polymers. ε_{ab} is always smaller than 1.0 to simulate two immiscible polymers at different degrees of wetting, the planar interface is therefore stable throughout the simulation. A series of analyses are conducted after equilibrating the system for 15 million simulation steps, we refer this stage as analysis of static state. The system was then sheared by imposing velocity profile through explicit walls, and analysis of shearing state as conducted after continuously shearing for 15 million steps.

4.3.1 Interface Structure

Despite the fact that polymers are made immiscible, there is still interpenetration at the interface that causes the interface to contain both types of polymers. We divided our simulation into layered bins, each of thickness 0.5σ, along z direction, and compute the number ratio of each species of particles. As in Figure 22, two polymers formed an intermediate region that composes of both polymers, which is indicated by non-zero ratio value of both polymers. In the simulated system, lower layers (smaller *z*) are exclusively polymer A, but polymer B start to appear once *z* increases to interface region, upon further increasing the *z* coordinates, the top region is exclusively B polymers. The ratios of fillers show a strong peak at the interface indicating migration of fillers as a result of minimizing free energy; the magnitude of the peak should however not be compared for different types of the fillers, since number fraction is used instead of the volume fraction.

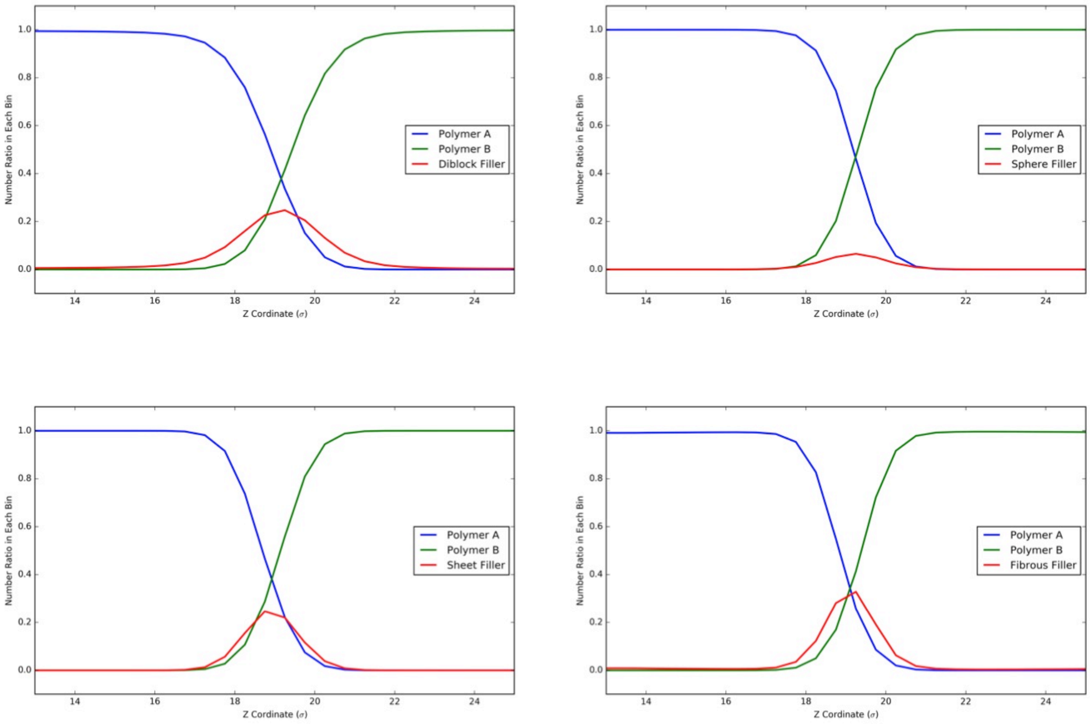

Figure 22. Particle composition at each bin along z direction. (Pictures show only the regions close to interface). (a). Polymer blends with diblock fillers. (b) Polymer blends with spherical fillers. (c) Polymer blends with sheet (platelet) fillers. (d). Polymer blends with fibrous fillers. The pictures here represents systems with 2% fillers, ε_{ab}=0.7 and ε_{fp}=1.0.

The interfacial structures, however, are very different depending on the type of fillers and are extremely sensitive to the interactions between polymer and filler. The two ends of diblock fillers penetrated deeply into both two polymers phases at larger filler-polymer interaction ε_{fp}=2.0, as can be seen in Figure 23b. It is obvious from Figure 23c that the number ratios of diblock copolymer in each layer are almost the same, since the diblock polymers are fully stretched at ε_{fp}=2.0. In contrast, diblock copolymer shrinks into mushroom like structures at a weaker interaction ε_{fp}=1.0 (Figure 23b) with most of them aggregated at the polymer interface. Majority of the spherical fillers migrates to the interface at ε_{fp}=1.0 (Figure 23a), but a significant portion of spherical fillers remains in polymer phase when ε_{fp}=2.0 (Figure 23b). It is also shown in Figure 24c, the number ratio of spherical fillers at the interface is much higher when ε_{fp}=1.0. Platelet filler is strongly affected by the filler-polymer interaction, at ε_{fp}=1.0, platelet fillers lie at the interface as an attempt to reduce the contact area of polymer A-B (Figure 25a). Platelet fillers intercalated with polymers when filler-polymer interaction ε_{fp} increased to 2.0 (Figure 25b). A significant amount of the intercalations moved to the interface and stand vertically. As a result, the number ratio of platelet fillers at the interface reduced significant as ε_{fp} increased to 2.0, but two shoulders appears since the side of platelet fillers penetrate into the polymer phase (Figure 25c). In Figure 26 a-b, we observe fibrous filler aligned into an ordered structure at the interface in both case. Figure 26c shows strong aggregation of fibrous fillers, at ε_{fp}=1.0, more than 40% of the particles at the interface are fibrous fillers. We note that fillers migrates to interface universally in Figure 23 to Figure 26, since polymer A-B interaction is at ε_{ab}=0.7 and filler-polymer interaction is consistently stronger, either at ε_{fp}=1.0 or at ε_{fp}=2.0. Fillers aggregate at the interface and arrange themselves in a way that best reduced the contact area of polymer A and polymer B, the structure is however subject to the entropy penalty which depends on the shape of fillers and subject to the interaction of filler-polymers.

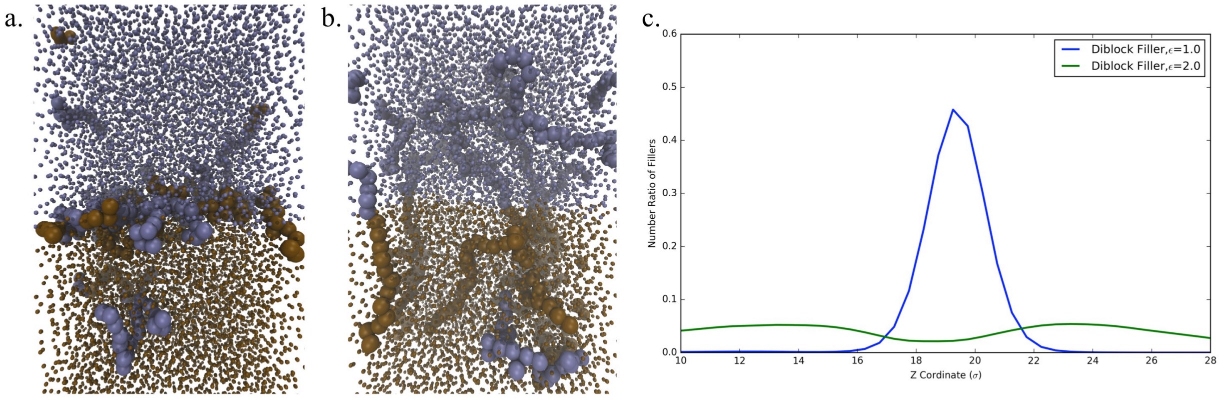

Figure 23. (a). Interfacial structure of diblock copolymer fillers at ε_{fp}=1.0. (b). Interfacial structure of diblock copolymer fillers at ε_{fp}=2.0. (c). Number ratio of diblock particles in layered bins. The system has 3% fillers and ε_{ab}=0.7.

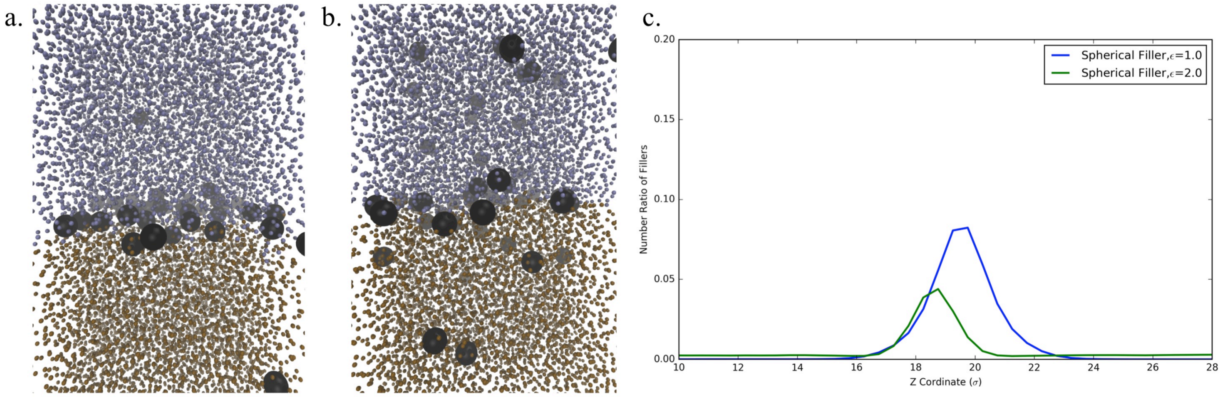

Figure 24. (a). Interfacial structure of spherical fillers at ε_{fp}=1.0. (b). Interfacial structure of spherical fillers at ε_{fp}=2.0. (c). Number ratio of spherical particles in layered bins. The system has 3% fillers and ε_{ab}=0.7.

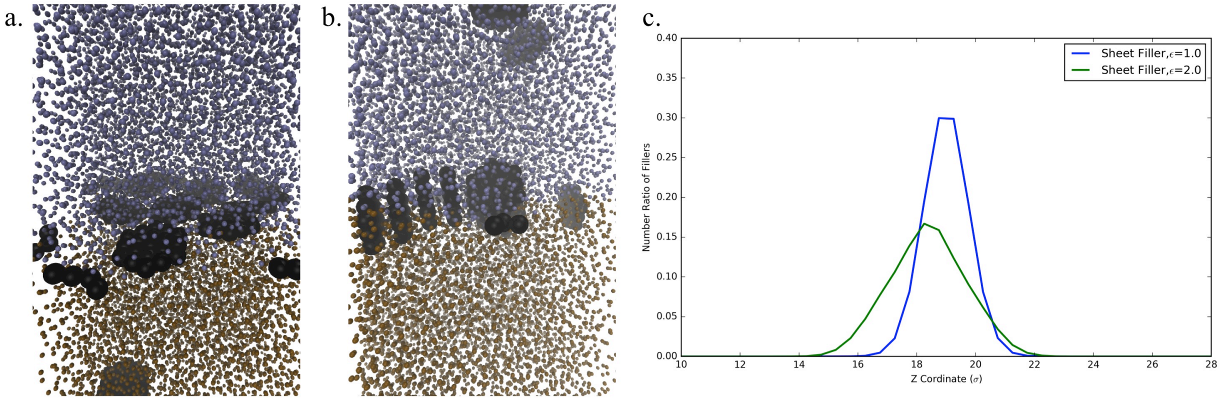

Figure 25. (a). Interfacial structure of platelet fillers at ε_{fp}=1.0 (b). Interfacial structure of platelet fillers at ε_{fp}=2.0 (c). Number ratio of platelet filler particles in layered bins. The system has 3% fillers and ε_{ab}=0.7.

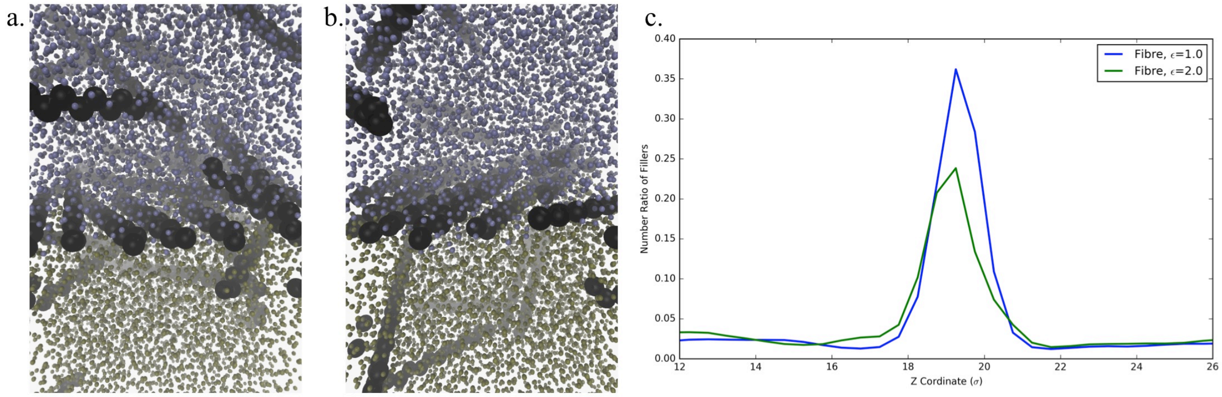

Figure 26. (a). Interfacial structure of fibrous fillers at ε_{fp}=1.0 (b). Interfacial structure of fibrous fillers at ε_{fp}=2.0 (c). Number ratio of fibrous filler particles in layered bins. The system has 3% fillers and ε_{ab}=0.7.

4.3.2 Interfacial Tension

Interfacial tension is the most direct quantity to measure the interfacial compatibility of two materials. In MD simulation, it's possible to calculate, as discussed in method section, the interfacial tension by integrating the difference between normal pressure and tangential pressure for a system with planar interface. We divide our simulation domain into layers along z direction, and calculated pressure difference γ of each layer by Equation 31. Results of γ are presented in Figure 27 for polymer blends of different miscibility ε_{ab}. It's obvious from the picture, γ is equal to 0 in layers that are far from the interface and can therefore be safely neglected. A significant peak of γ raised at the interface, indicating there is strong interfacial tension between two polymers. The peak increases as a react to decreased miscibility (smaller ε_{ab}). In Table 1, we calculated the interfacial tension of those systems in Figure 27, the interfacial tension steadily increased as ε_{ab} getting smaller. The results prove that ε_{ab} effectively control of the compatibility between two polymers and Equation 31 provides qualitatively good measuring of the interfacial tension.

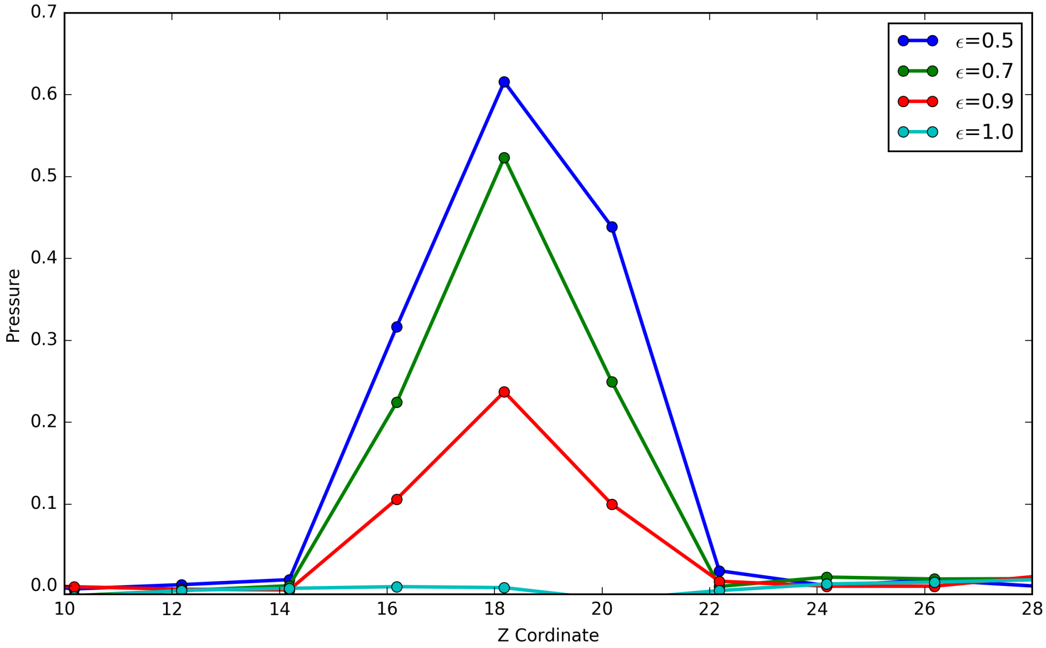

Figure 27. Pressure difference γ at different polymer A-B interaction (ε_{ab}). The simulation domain is divided into layers of thickness 1.5σ along the z direction.

Table 1. Interfacial tension of polymer blends at different polymer A-to-B interactions (ε_{ab}).

ε_{ab}	1.0	0.9	0.7	0.5
Interfacial Tension (ε)	0.03	0.45	1.03	1.40

Nanofillers modified the interface of two polymers and therefore changed the interfacial tension. In Figure 28 we show the interfacial tension of the polymer blends with different concentration of fillers. Surprisingly, the fibrous and platelet fillers almost have no effect on the interfacial tension at weak filler-polymer interaction ε_{fp}=1.0 (Figure 28a), in contrast, diblock filler shows great reduction on the interfacial tension. We think this is because the interaction between finite sized filler particles and polymers has to be larger to achieve same degree of wettings as the diblock copolymers. At ε_{fp}=1.0, the two ends of diblock copolymer is indeed indistinguishable from two polymers. Significant changes occurred once ε_{fp} increased to 2.0, the diblock filler almost show no effects on interfacial tension, this can be explained by the structure in Figure 23b, where we saw diblock copolymer stretched and only a tiny fraction of diblock copolymer particles present at the interface. The platelet filler, fibrous filler and spherical fillers all shows significant reduction on the interfacial tension when ε_{fp}=2.0, the rate of reduction however reduced when filler concentration increased to 3.0% due to the saturation of fillers at the interface. It should be noted that the aggregation of spherical fillers at the interface disturbed the pressure tensor severely when ε_{fp}=1.0, and we observe double peak formed in the pressure difference γ curve. This phenomenon could be explained by the large unit size of the spherical fillers (twice in diameter than unit spheres). At weak polymer-filler interaction, spherical fillers formed a thick layer at the interface that lacks of polymer particles. We think this double peak of pressure curve might make the interfacial calculation invalid, so the result is not presented. It is also worth to note, inclusion of platelet and fibrous fillers also brings perturbations to the pressure tensor at the interface, as a result, the interfacial tensions show wild fluctuation as in Figure 28.

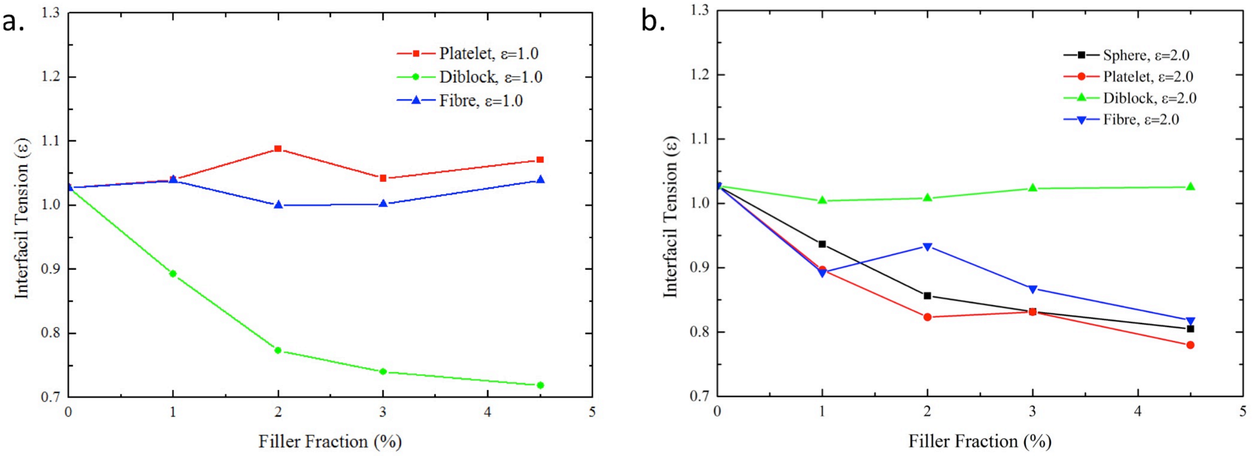

Figure 28. Interfacial tension of the polymer blends with different fillers. (a) Filler-polymer interaction at ε_{fp}=1.0. (b) Filler-polymer interaction at ε_{fp}=2.0. The miscibility of two polymer is both at ε_{ab}=0.7.

4.3.3 Interfacial Slip

When polymer blends are subjected to external shearing, slip could occur at interface due to insufficient adhesion between two polymers. We impose shearing by moving the top and bottom wall at constant speed 0.48σ/τ and in opposite directions. This shearing speed correspond to a considerably large shearing force which cause interfacial slippery for most of the systems. Addition of nanofillers significantly improves the shear-resistance of the polymer blends. At ε_{fp}=1.0, platelet fillers, fibrous fillers and diblock copolymer fillers all significantly reduced the interfacial slip, as shown in Figure 29. The only exception is the spherical fillers (not included in Figure 29), where we observed almost doubled slip length, this is a result due to the creation of a thick layer of spherical fillers at the interface which have little adhesion to the polymers and have little space constraints when ε_{fp}=1.0.

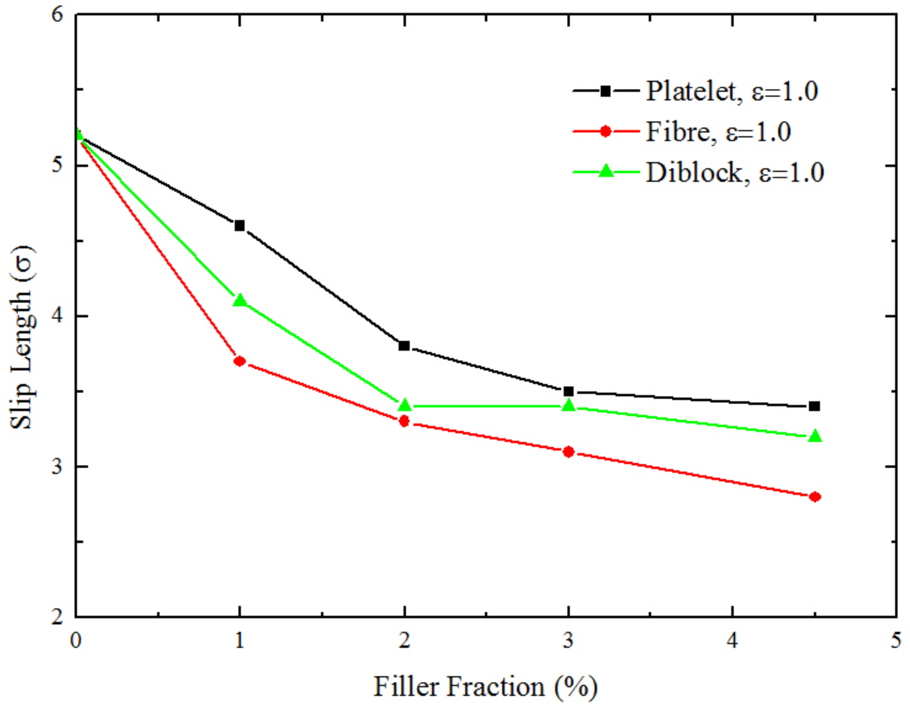

Figure 29. Interfacial slip length of polymer blends with fillers at filler-polymer interaction ε_{fp}=1.0. The miscibility of two polymers is ε_{ab}=0.7 and the shearing is at constant speed 0.48σ/τ.

The effect of nanofillers on polymer blends is much more significant when filler-polymer interaction increased to ε_{fp}=2.0. We saw the slip length are further reduced (Figure 30) compared to those with ε_{fp}=1.0 (Figure 29), addition of 3.0% platelet filler or fibrous fillers reduce the interfacial slip length by more than 50%. Even with spherical fillers, we observe a consideration reduction on the interfacial slip length. However, the effects of platelet fillers and fibrous fillers are obviously better than that of spherical fillers, we think it is a results of the ordered structure formed by platelet and fibrous fillers at the interface (Figure 25 and Figure 26). The formation of such ordered structure offers higher constraints to the motion of platelet and fibrous fillers and therefore provides extra frictions to the polymers. The rate of reduction slowed down at about 3.0% of fillers, which is a result of saturation of fillers at the interfacial plane. The diblock copolymer actually shows the most significant effect on shear-resistance. We observe an almost continuous velocity profile with only 1.0% diblock copolymer (Figure 31), adding more diblock copolymers cause fluctuation at the mid region but it is different from a velocity profile where interfacial slip occurs. It is a special result of diblock copolymer penetrates deeply into polymers (Figure 23) and strongly entangled with polymers at ε_{fp}=2.0. Streching two ends of the diblock copolymers to opposite direction cause the velocity to fluctuate at the mid point. We conclude there is no slippery in those systems.

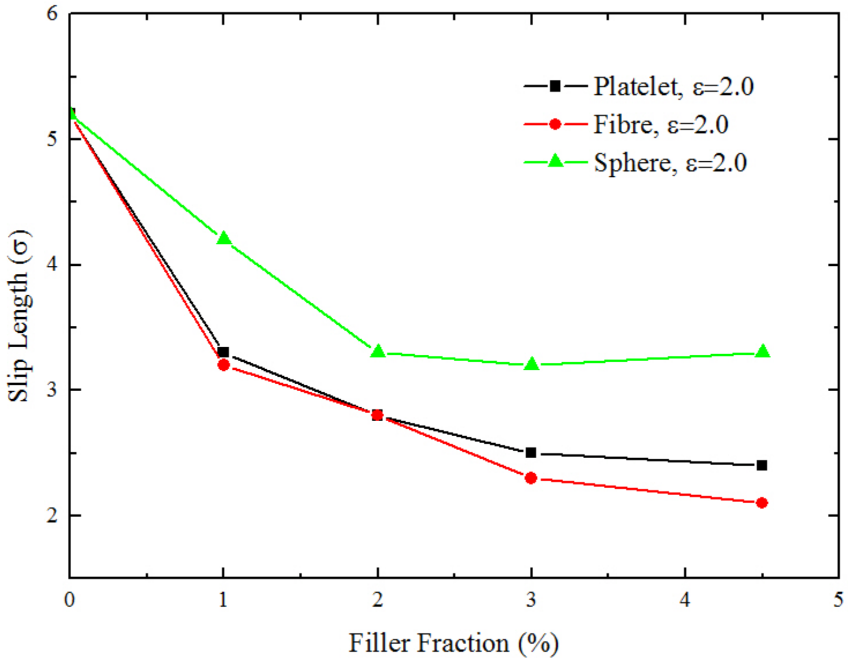

Figure 30. Interfacial slip length of polymer blends with fillers at filler-polymer interaction ε_{fp}=2.0. The miscibility of two polymers is ε_{ab}=0.7 and the shearing is at constant speed $0.48\sigma/\tau$.

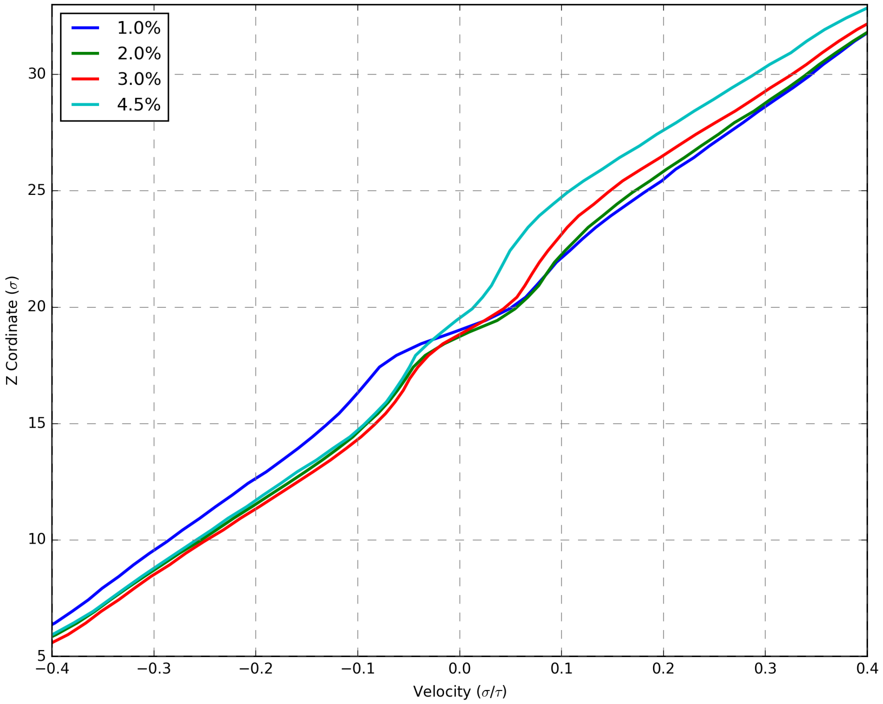

Figure 31. Velocity profile of polymer blend with diblock copolymer fillers at filler-polymer interaction ε_{fp}=2.0. The miscibility of two polymers is ε_{ab}=0.7 and the shearing is at constant speed 0.48σ/τ.

4.4 Conclusion

We constructed a model of two immiscible polymers with a planar interface to study the effects of nanofillers on the interfacial behavior of the nanocomposite. We found the interaction between filler and polymer strongly affects the interfacial structure. Diblock copolymer stretched into two polymer domains at strong filler-polymer interaction ε_{fp}=2.0, platelet fillers aggregates into intercalated structure at ε_{fp}=2.0 and some of these intercalation stand vertically at the interface, and fibrous fillers aligned at the interface at both ε_{fp}=1.0 and ε_{fp}=2.0. As a result of different interfacial structure, the interfacial properties are quite different from case to case. Platelet, fibrous and spherical filler reduce the interfacial energy only when the filler-polymer interaction is strong. The diblock copolymer however shows the opposite trend, it reduce the interfacial tension significantly by aggregating at the interface when ε_{fp}=1.0. The diblock copolymers however penetrate to polymer domains and therefore has not effect on interfacial energy when ε_{fp}=2.0. The mechanism of nanofiller in preventing interfacial slip is very different from reducing the interfacial tension. Platelet fillers and fibrous fillers show much more improvements on the shear resistance than spherical filler, this is mainly due to the ordered structure they formed at the interface. Stronger filler-polymer interaction leads to more significant improvements on shear resistance. At ε_{fp}=2.0, 3.0% of platelet or fibrous fillers reduce the slip length by more than 50%. Adding 1.0% of diblock copolymers prevent the interfacial slip when ε_{fp}=2.0, since the diblock copolymer entangled strongly with the polymers.

Chapter 5. Self-assembly of Polymer Blends for Solar Cells

5.1 Introduction

With increasing concerns about a looming energy crisis and global warming, studies on clean and renewable energy have drawn a great deal of attention. Solar energy is one of the most popular candidates due to its abundant supply and great accessibility. Humans have been utilizing sunlight for a long history, but it was not until first solar cell was invented in mid last century, that we were finally able to convert sunlight to the most useful form of energy: electricity.[134] We now find solar cells widely used in space engineering, in portable devices and even used as the primary electricity resource in some remote areas.[135-137] The prevailing solar cell products presently on the market are mostly based on silicon wafers, which suffer from the high cost of silicon raw materials.[138] The more recent invention of polymer solar cell (PSC) provides a cost effective alternative to silicon-based solar cells, while also having the advantage of being lightweight and flexible.[139]

Polymer solar cells usually consist of two components, one as the electron donor and the other as electron acceptor. Photons with high enough energy are adsorbed by the photovoltaic polymer and excite electrons from their ground state to generate electron-hole pairs.[140] By engineering an acceptor, typically a fullerene, the electron-hole pair separates at the donor-acceptor interface and diffuses to two electrodes respectively.[141-143] Researchers have been engaged to invent new PSC with better performance, especially to improve the conversion efficiency. It is now understood that a large interfacial area for electron-hole separation and a continuous pathway for electron and hole transport are crucial factors for a high performance PSC.[144] Bulk heterojunction thin film is among one the most popular active layer structure being used now.[145] In bulk heterojunction thin film, donor and acceptor interpenetrate each other, the active layer therefore has a large interfacial area for electron-hole pair separations. However, the randomness of the interpenetration impedes the transportation of electrons and holes, a significant portion of electrons are blocked at the bottlenecks, and the convoluted travel routes also increase the diffusion distance.[144,146]

Self-assembly of polymer blends provide an alternative route for controlled fabrication at nanometer scale and is promising to applied to PSC active layer. In recent work we have proposed a novel approach that introduces polystyrene to organize the poly(3-hexylthiophene) (P3HT) into columnar phases decorated by [6,6]-phenyl C_{61}-butyric acid methyl ester (PCBM) at the interface, as in Figure 32.[147] This structure represents a realization of an idealized morphology of an organic solar cell, in which both exiciton dissociation and the carrier transport are optimized, leading to high power conversion efficiency. In this chapter, we analyzed from theoretical point of view the formation of such a columnar structure in a polymer binary blend subject to thin film environments. We investigate the miscibility of two polymers, affinity of nanofillers to polymers and the thin film confinement by using a molecular dynamics model.

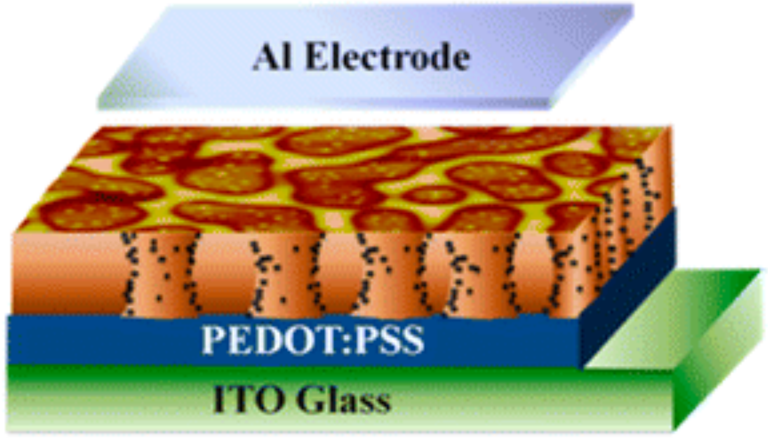

Figure 32. Schematic showing the structure of the modified BHJ solar cell.[147] The surface image was obtained from the two-dimensional AFM scan of the film coated onto the PEDOT:PSS layer.

5.2 Model and Methods

Our molecular dynamics simulation model used simple bead-spring model to simulate two immiscible polymers, labeled as A and B, confined to a thin film domain. All the quantities in the simulation are reduced to a dimensionless format by letting energy unit ε, distance unit σ, and Boltzmann constant k_b all equal 1. We used standard velocity-Verlet time integration with step length $\Delta t=0.005\tau$. To simulate the thin film geometry, particle walls are imposed to the simulation domain on both top and bottom. Each wall is made of two layers of Lenard Jones spheres densely packed in fcc(111) lattice and moves as an entity.

The monomers of the polymer chain interact with each other by a modified Lennard-Jones potential of the form:

$$V^{LJ}(r)=\begin{cases}4\varepsilon\left[\left(\frac{\sigma}{r-\Delta}\right)^{12}-\delta\left(\frac{\sigma}{r-\Delta}\right)^{6}\right], & r\le r_c+\Delta\\ 0, & r\ge r_c+\Delta\end{cases} \tag{32}$$

standard cutoff $r_c=2.5\sigma$ is used for all pairwise interactions. An energy modification parameter δ is used to control the affinity of particles, e.g. when $\delta_{AB}<1$ for polymer A and B, the repulsive term in the LJ potential dominates and the two polymers become immiscible, δ by default is 1 if not otherwise mentioned. Δ is used to shift the potential to account for finite sized spheres of different size, we use constantly $\Delta=1.0\sigma$ for nanofillers pairs, $\Delta=0.5\sigma$ for filler to polymer interactions and $\Delta=0$ for all other pairs. The Δ values we use simulate nanofillers with effective diameter 2.0σ. When $\delta=1$ and $\Delta=0$, the equation actually reduced back to standard form of LJ 12-6 equation. The potential well depth $\varepsilon=1$ for all pairs except that ε_{fp} between the polymer and the nanofillers varies between 1.0-2.0.

Both polymers consist of linear chains, each with 32 segments, which correspond to polymers below the entanglement length found in literature. Adjacent monomers along the chain are bonded by an additional FENE potential of the form:

$$V^{bond}(r)=\begin{cases}0.5R_0^2 k\ln\left[1-\left(\frac{r}{R_0}\right)^2\right], & r\le R_0\\ \infty, & r>R_0\end{cases} \tag{33}$$

in which elastic constant k = 30 and maximum extensible length $R_0=1.5\sigma$.

If not otherwise mentioned, we used a system of size $32\text{x}32\text{x}16\sigma$ of x, y and z directions respectively; the overall number of monomer is 16384. The simulation box was chosen such that the thickness was roughly 7 times the radius of gyration of the polymers (as was used in the experiments). We used periodic boundary conditions in the x and y directions, while the z direction was bounded by walls. The interaction parameter, ε, between the wall atoms and the polymers and the nanofillers was fixed at $\varepsilon=4.0$. We used a fifth order predictor corrector algorithm with a time interval of $t=0.005\tau$. Constant temperature was maintained at $T=1.1(k_b/\varepsilon)$ by using a Langevin thermostat.

5.3 Results and Discussion

For the first set of simulations, we used volume fraction of filler ranging from Φ=0.0%, 3.13%, and 12.52%. The number ratio of polymer A (non-photoactive) and B was kept constant as 403:108, roughly equal to 20% of polymer B. We introduced a slight repulsion between the two polymers by setting $\delta_{AB} = 0.75$ and kept the interaction between the nanoparticle and the two polymers to be identical (at ε=2.0). In all these simulations we started from a completely mixed state (δ = 1.0) and then equilibrated the system (NPT) for at least 8 million time steps. Once our system was equilibrated, and we determined this by monitoring the radius of gyration of the chains (R_g), and the diffusion of the center of mass of the polymer (on the order of several R_g), we then reduced the value of δ_{AB} to 0.75 and further equilibrated for another 8 million time steps, under NVT condition.

Snapshots of our system at different timesteps are shown in Figure 33 (only snapshot of Φ=3.13% was presented due to similar results of these systems). As can be seen from the figure, an initially mixed state evolves into two columnar phases, which ultimately merge into a single columnar structure. It's obvious that columnar structure is a nature result of phase separation of two immiscible polymers; the process therefore would depend on both segregation time and immiscibility of two polymers. We prove this by estimating the interfacial area with number of interface particles and investigate it as a function of both time and $\delta_{AB,}$ Figure 34. It's obvious that interface area keeps decreasing as a result of phase segregation, the rate and completion of phase separation is proportional to the immiscibility of two polymers.

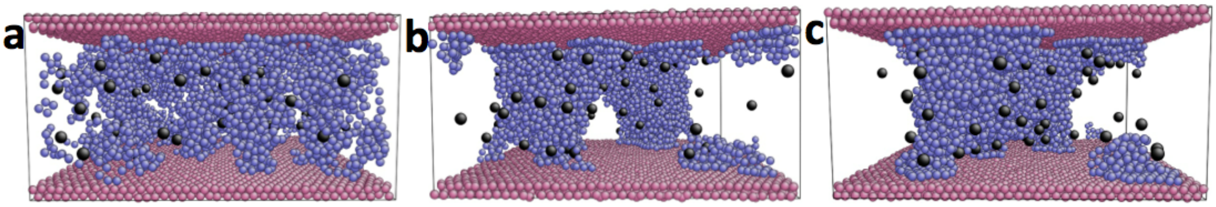

Figure 33. Snapshot at different simulation steps of simulation system with Φ=3.13%, δ=0.75, δ_f=1.0. Non-photoactive polymer A was hidden. (a) Initial state before phase separation. (b) Snapshot at 4 million time steps. (c) Snapshot at 8 million time steps.

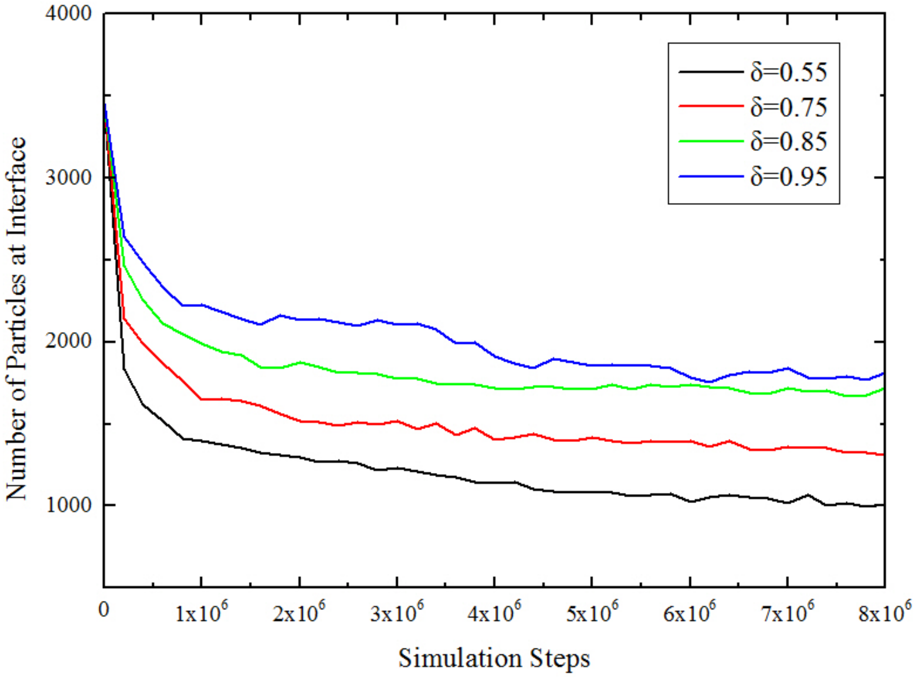

Figure 34. Number of polymer B particles at the interface at different simulation steps. The δ_{AB} between two polymers are 0.55, 0.75, 0.85 and 0.95 from top to bottom respectively, no nanofillers are included in these systems.

What should also be noted from Figure 33 is that most of the nanoparticles tend to segregate to the interface between the two phases. For most of the simulations that we have run (starting from 3-5 random initial states), we see the system starting off with multiple columns and then merging into one, as would be expected during phase separation. However we see instances in systems with Φ=12.52%, the two columns do not merge in 8 millions time steps which hadn't been discovered in other two Φ value systems we simulated. We think this is a result that is also expected, as a larger number of fillers (segregated to the interface) can lower the local interfacial tension and possibly stabilize multiple columns. If even higher concentration of filler at Φ=25.04%(All other parameters remain) were used, we see this phenomena again (as expected), in Figure 35. The two columns persist even after twice the normal equilibration time (to 16 million time steps). We concede this is a function of the initial starting point, and so is not an equilibrium structure, as even at these higher concentrations we see merging into a single column. However, we anticipate that in the experimental results, since the chains are longer and kinetic effects are more pronounced, we will always see multiple columns. It is important to recognize, that in all cases, these columns span the complete thickness of the film, and the nanoparticles segregate to the interface between the polymers.

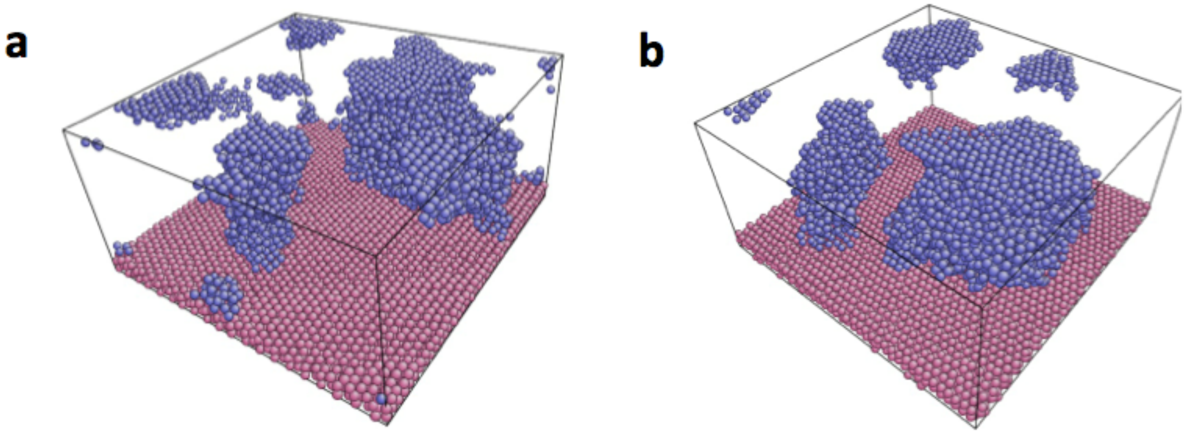

Figure 35. Morphology of MD simulation system with Φ=25.04%, δ=0.75, δ_f=1.0. The top wall has been removed and only the photoactive polymers (blue) were shown for clarity. The angle of view was chose so that the columnar structure (red circles) could be seen best. (a) Snapshot at 8 million time steps. (b) Snapshot at 16 million time steps.

For the next set of simulations, we examined the effect of changing the interaction between the nanoparticle and the polymer phases. We chose an interaction that made the nanoparticle slightly repulsive to one phase (the non-photoactive polymer), by introducing a parameter δ_f, which reduces the attractive portion of the LJ potential. Any value of $\delta_f < 1$ denotes a repulsive interaction between the nanoparticle and the non-photoactive phase. We perform our usual equilibration procedure for filler volume fraction Φ=12.52%. Then we used two sets of parameters, a. δ_{AB}=0.75, δ_f=1.0, b. δ_{AB}=0.75, δ_f=0.9. As can be seen from the snapshots after 8 million time steps (figure 3), far more nanoparticles are localized at the interface between the two phases with δ_f=0.9. To quantify the localization of the nanoparticles we constructed a simulation geometry in which we have a system with polymer A on top, and polymer B at the bottom (Inset in Figure 37). We divided the simulation box into 16 partitions along z direction and plot the time average of filler fractions in each partition (Figure 37). As we decrease the value of δ_f, we notice that almost all the nanoparticles are now present in the photoactive polymer. However, at lower values of δ, the amount of nanofiller at the interface decreases, implying that there is an optimum value of interactions that can be tailored by choosing the non-photoactive polymer appropriately.

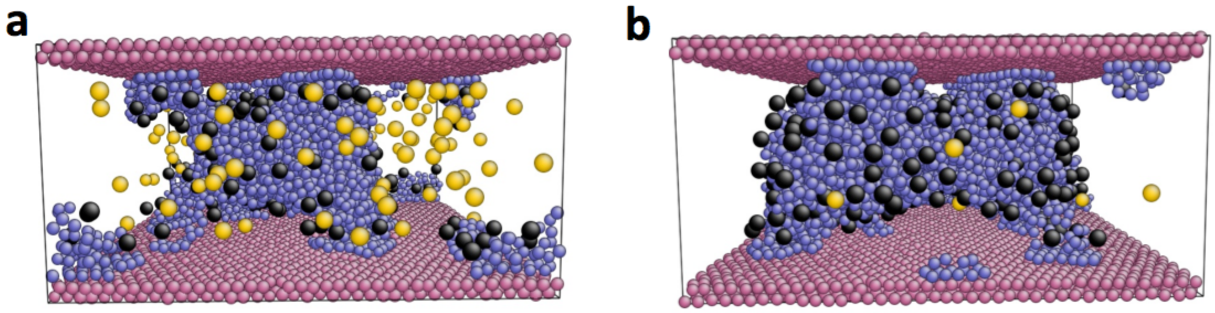

Figure 36.Snapshot of simulation systems (Φ=12.52%, δ=0.75, but with different δ_f) at 8 million time steps. Nano-filler at A-B interface were black colored, while those distributed in A phase (non-photoactive) were yellow colored. (a) Simulation system with δ_f=1.0. (b) Simulation systems with δ_f=0.9.

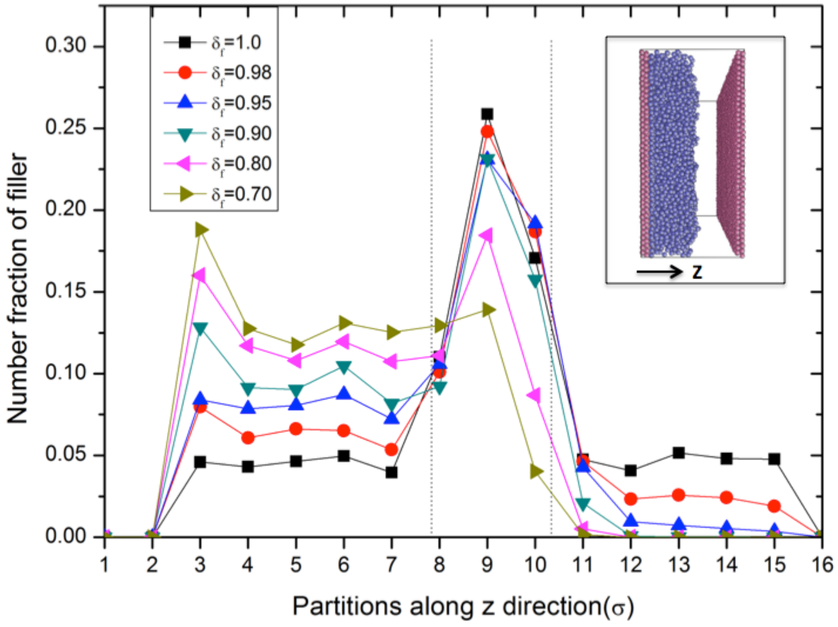

Figure 37. Number fraction of fillers in each partition along z direction (x axle is the sequence number of the partition). δ_{AB}=0.75 between polymer A and B, volume fraction of filler Φ=12.52%. The inset picture shows the geometry of polymer A and B that were used in this test.

Our simulation results show controlled nanostructure can be achieved with simple self-assembly in a PSC thin film. Guided by the simulations, Dr Rafailovich's group synthesized PS/P3HT/PCBM solar cell and used TEM to investigate the column formation by looking at the cross-section of the thin film; Figure 38 shows clearly the formation of column structure in such polymer blends. They also used neutron scattering to show the migration of PCBM particles into the interface of PS and P3HT. We refer to the paper for more about this study.[146] The simulation results provide a theoretical support for controlled nano morphology by tuning some simple physics of polymers. Together with the experimental results, it's obvious that two immiscible polymers can achieve controlled column structure in a confined thin film system, which could improve the performance of polymer solar cells.

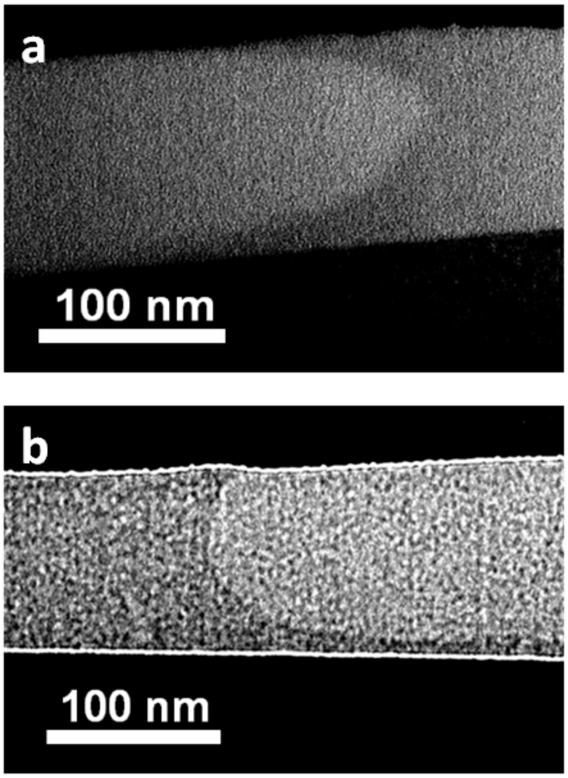

Figure 38. TEM images of focused ion beam cross sections obtained from films spun cast on HF etched Si wafers at 700rpm; (a) The 1:1 weight ratio PS / P3HT binary blend film and (b) the 1:1:1 weight ratio PS, P3HT and PCBM tertiary blend film.[146]

The generation of electrical current for solar cells requires continuous path for electrons and holes to transport to electrodes, the conversion efficiency is therefore impacted by the percolating columnar structure. We further investigate the effects of thin film thickness and miscibility of two polymers on the percolating column structure. It should be noted, a slightly different model were used for the followed simulations. We summarize the main difference in this paragraph. Classical LJ potential was used instead in this model

$$V^{LJ}(r) = \begin{cases} 4\varepsilon\left[\left(\frac{\sigma}{r}\right)^{12} - \left(\frac{\sigma}{r}\right)^{6}\right], & r \leq r_c \\ 0, & r \geq r_c \end{cases}$$

We tune the miscibility of two polymers by varying $\varepsilon_{\mathrm{AB}}$ between the two types of particles from 0.5-1.0, smaller $\varepsilon_{\mathrm{AB}}$ models polymers that are more immiscible. The polymers are simulated with FENE potential and same parameters; however, we used smaller chain length that equals to 8. The composition of two polymer is hold the same, which is 20% polymer B and 80% polymer, but we adjust the thickness of simulated system by adding more polymer particles to it. The model also scaled up than the previous one: this model has larger x and y dimension both at 60σ, and simulation runs for much longer steps, all results presented are after 25 millions simulation steps ($1.25\times10^{5}\tau$).

Stable percolating columnar structures were observed in simulations where $\varepsilon_{\mathrm{AB}}$ is equals to 0.5 and the thickness of the simulated system is 27σ, as shown in Figure 39a. As we improved the miscibility of two polymers by changing $\varepsilon_{\mathrm{AB}}$ to 0.9, columnar structure still forms but the phase segregation are more incomplete than what we have when $\varepsilon_{\mathrm{AB}}$-0.5, indicating by many suspending clusters, shown in Figure 39b. As we increase the system thickness to 35σ but hold two polymers to be very immiscible with $\varepsilon_{\mathrm{AB}}=0.5$, columnar structures were still observed as shown in Figure 39c. However, if we increase the miscibility, the columnar structure breaks and hemisphere aggregation to both walls were observed instead (Figure 39d). When we further increasing the thickness to 43σ, columnar structures are not formed in both degree of miscibility (Figure 39 e and f). The results prove that columnar structure is sensitive to both miscibility of two polymers and the thin film thickness. Decreased miscibility of two polymers accelerates the phase segregation and helps to form more regular columnar structures. When thin film thickness increase, the simulated photovoltaic polymer aggregates into two thin film boundaries, which is a more stable state at this thin film thickness.

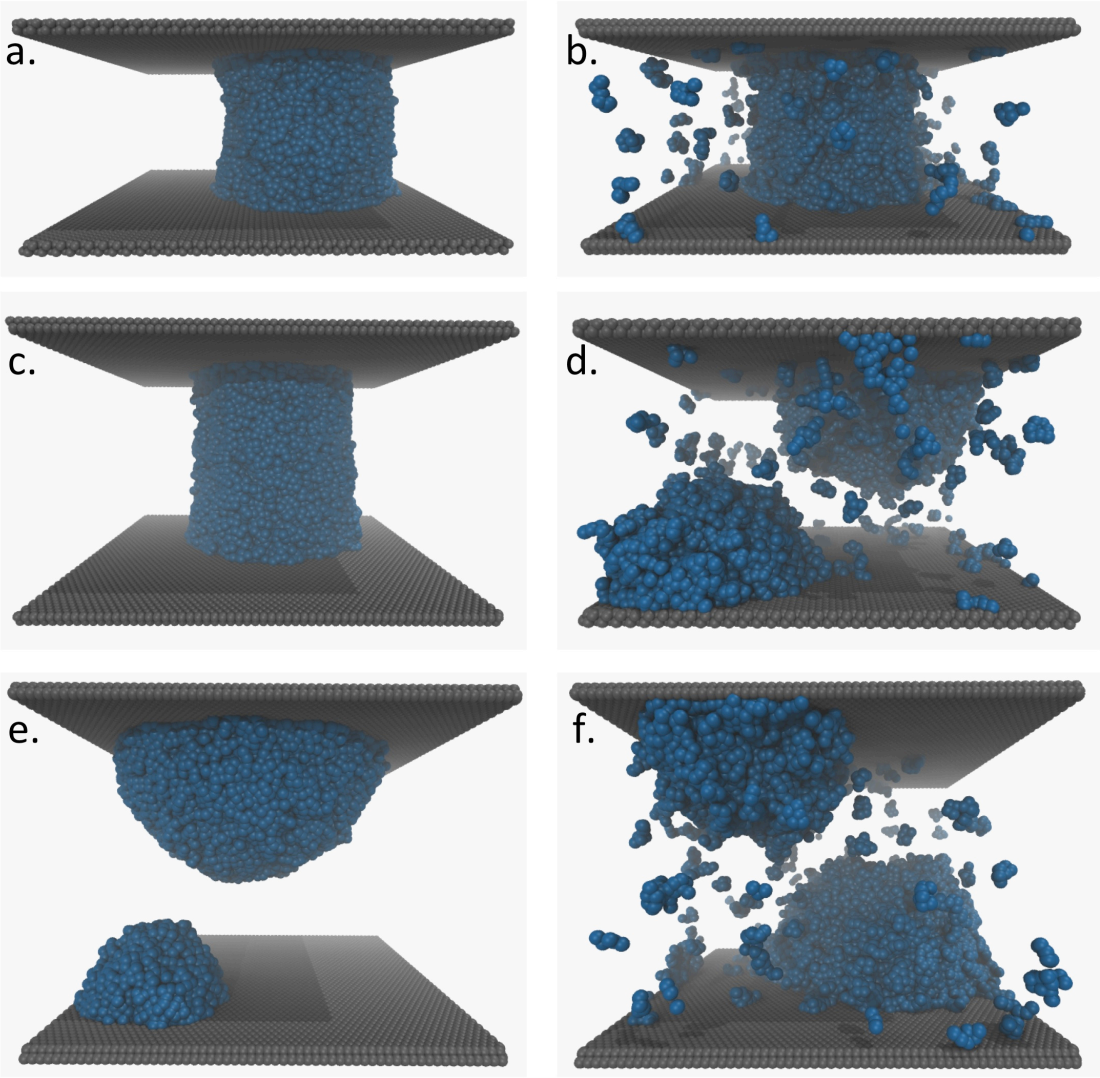

Figure 39. Molecular structure of immiscible polymer blends in a thin film, at different miscibility ε_{AB} and different thin film thickness (T) (a).ε_{AB}=0.5, T=27σ. (b).ε_{AB}=0.9, T=27σ. (c).ε_{AB}=0.5, T=35σ. (d).ε_{AB}=0.9, T=35σ. (e).ε_{AB}=0.5, T=43σ. (f).ε_{AB}=0.9, T=43σ.

Limited by the finite size of our simulation domain, the simulated structure may represent only a small chunk of the real PSC thin film, and the final structure also shows dependency on the initial simulation morphology. We therefore conducted 3 simulations for each combination of ε_{AB} and thickness and summarize the results as a phase diagram in Figure 40. From the phase diagram, it's obvious that percolating columns are more likely to form in thinner film, the columns breaks into non-percolating bulks at thicker film or if the miscibility of two polymers improved. There are obviously other factors that affect column formation, such as temperature and polymer ratio, the simulation results nonetheless sufficiently proved that the column formation is driven by the interfacial tension between two polymers and is a particular result of thin film confinements.

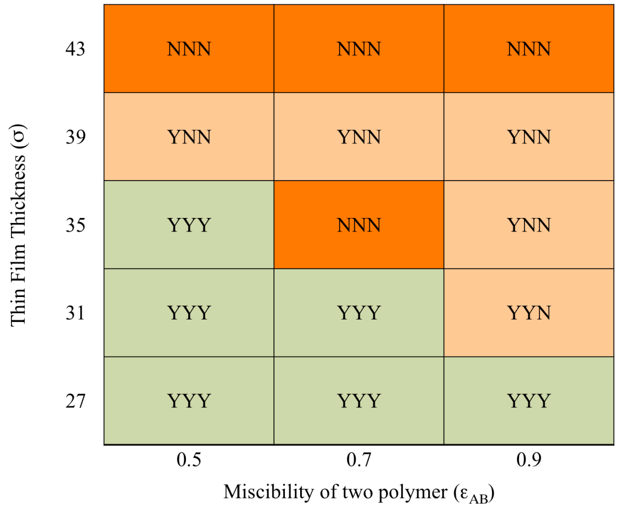

Thin Film Thickness (σ)	0.5	0.7	0.9
43	NNN	NNN	NNN
39	YNN	YNN	YNN
35	YYY	NNN	YNN
31	YYY	YYY	YYN
27	YYY	YYY	YYY

Figure 40. Percolating column structure formation in simulations of different parameter settings. Three simulations were conducted for each combination of film thickness and ε_{AB}, Y/N denote percolating column structure is observed or not, respectively.

Guided by simulation results, Dr. Rafailovich's research group investigate this self-assembled PSC with series of experiments, they select PMMA instead of PS to synthesize PMMA/P3HT/PCBM PSC thin film, since PMMA/P3HT is much more immiscible than PS/P3HT blends. The experiment results perfectly consistent with our simulations, they not only found columns of P3HT, but the conversion efficiency of such composite thin film is very satisfactory compared with a typical BHJ polymer solar cells. In a bulk heterojunction thin film PSCs, the increased thickness would harm the conversion efficient since the transportation of electrons and holes were impeded by the irregular interpenetration structure. However, this self-assembled PSC has increasing conversion efficiency with thickness due to more photovoltaic materials added and much more controlled percolating columns structure. The performance of such PSC only starts to drop down when thickness was increased to as high as 600 *nm*s, due to the breaks of columns structure.

5.4 Conclusions

We used MD model to show two immiscible polymers can form percolated column structure when confined to a thin film. By selecting nanofillers (or small polymers) with proper affinities to each polymer, a controlled nanostructure with percolating polymer columns and the nanofillers segregating mainly at the interface could be achieved. This kind of structure was greatly appreciated by a polymer solar cell thin film, in which continuous path for electrons transport and large interfacial area for electron-hole separation are critical for good energy conversion efficiency. The percolating column formation is sensitive to both miscibility of two polymers and thickness of the thin film. More stable columns, yet more complete phase segregation of polymers, were achieved with more immiscible polymers under critical thickness. The columns are more apt to break when the thickness of thin film were increased, this was shown as a statistical phase diagram. Our results are useful to select proper polymer blends to fabricate self-assembled polymer solar cell thin film with preferable nanostructure and better electrical performance.

6. Future work

The nanoplatelet fillers we simulated are limited to a small dimension with aspect ratio about 5, a much larger platelet model will be used to fully investigated the effects of anisotropic filler. The physical bonding in our model is also limited to end-monomer and each of the sphere particles in the platelet filler. We think the structure of gel network will be affected by the distribution of functional monomers along the polymer chains. It is also worthwhile to investigate how the distribution of functional sites in the platelets will affect the structure and properties of the composites gel. We will also investigate how the hydrodynamics will change the structure of such composite gel. Silicates filler, as common platelet filler, is usually charged on both the surface and the rim. We will eventually investigate the effects of charge and extends the study to cover electrolyte gels.

The structure of fillers at the interface of polymer blends is more complicated than we used to think. The effects of fillers on polymer blends are a strong function of their shape. We will have more simulations of diblock copolymer fillers of different length, platelet fillers of different aspect ratios and nanofibrous fillers of different size, so that we could compare different type of fillers more accurately. We will also investigate how the nanofillers would change the critical shearing force at which slip occurs at the polymer interface. The planar interface offers the ease for extracting information at the interface, but also constraints us to a very small interface area, we also plan to scale up the simulation, so that a much larger interface can be constructed. We will also investigate, with more simulations, how the interaction between platelet fillers and polymers will affects the structure of platelet fillers and therefore affects the interfacial behaviors of polymer blends.

The conversion efficiency of polymer solar cells is very sensitive to the interfacial area and the transport path of electrons to the electrode. We showed that more immiscible polymers lead to more completed phase segregation, but it also means reduced interfacial area for electron-hole separation. A much larger model is required to give a statistically significant result of the optimum combination of thin film thickness and miscibility of two polymers. We will also investigate how the two thin film boundaries (the supporting surfaces) will change the behavior of columnar structure formation. More simulations with electron accepter materials (nanofillers) will be conducted to study how existence of fillers will impact the nanostructure of such PSC thin film. We will also investigate how the persistent length of polymers would change the columnar structure formation.

Reference

1. Flory, P. J., *Principles of polymer chemistry*. Cornell University Press: Ithaca,, 1953; p 672 p.
2. Flory, P. J. *Faraday Discussions of the Chemical Society* **1974,** 57, (0), 7-18.
3. Schmaljohann, D. *Advanced Drug Delivery Reviews* **2006,** 58, (15), 1655-1670.
4. Blomen, L. J. M. J.; Mugerwa, M. N., *Fuel cell systems*. Plenum Press: New York, 1993; p xix, 614 p.
5. Li, G.; Zhu, R.; Yang, Y. *Nat Photonics* **2012,** 6, (3), 153-161.
6. Njuguna, J.; Pielichowski, K.; Fan, J. *Woodhead Publ Mater* **2012**, 472-539.
7. Paul, D. R.; Robeson, L. M. *Polymer* **2008,** 49, (15), 3187-3204.
8. Zheng, Y. P.; Zheng, Y.; Ning, R. C. *Mater Lett* **2003,** 57, (19), 2940-2944.
9. Xu, Q.; Mao, C.; Liu, N.-N.; Zhu, J.-J.; Sheng, J. *Biosensors and Bioelectronics* **2006,** 22, (5), 768-773.
10. Gas, J.; Poddar, P.; Almand, J.; Srinath, S.; Srikanth, H. *Adv Funct Mater* **2006,** 16, (1), 71-75.
11. Rittigstein, P.; Torkelson, J. M. *J Polym Sci Pol Phys* **2006,** 44, (20), 2935-2943.
12. Moniruzzaman, M.; Winey, K. I. *Macromolecules* **2006,** 39, (16), 5194-5205.
13. Choi, S.; Park, J.; Hyun, W.; Kim, J.; Kim, J.; Lee, Y. B.; Song, C.; Hwang, H. J.; Kim, J. H.; Hyeon, T.; Kim, D. H. *Acs Nano* **2015,** 9, (6), 6626-6633.
14. Finegan, I. C.; Tibbetts, G. G.; Glasgow, D. G.; Ting, J. M.; Lake, M. L. *J Mater Sci* **2003,** 38, (16), 3485-3490.
15. Kashiwagi, T.; Du, F. M.; Douglas, J. F.; Winey, K. I.; Harris, R. H.; Shields, J. R. *Nat Mater* **2005,** 4, (12), 928-933.
16. Ramanathan, T.; Abdala, A. A.; Stankovich, S.; Dikin, D. A.; Herrera-Alonso, M.; Piner, R. D.; Adamson, D. H.; Schniepp, H. C.; Chen, X.; Ruoff, R. S.; Nguyen, S. T.; Aksay, I. A.; Prud'homme, R. K.; Brinson, L. C. *Nat Nanotechnol* **2008,** 3, (6), 327-331.
17. Noh, M. W.; Lee, D. C. *Polym Bull* **1999,** 42, (5), 619-626.
18. Chen, G. H.; Wu, C. L.; Weng, W. G.; Wu, D. J.; Yan, W. L. *Polymer* **2003,** 44, (6), 1781-1784.
19. Wang, X. L.; Gao, Y.; Mao, K. M.; Xue, G.; Chen, T. H.; Zhu, J. J.; Li, B. H.; Sun, P. C.; Jin, Q. H.; Ding, D. T.; Shi, A. C. *Macromolecules* **2006,** 39, (19), 6653-6660.
20. Hao, J. K.; Weiss, R. A. *Polymer* **2013,** 54, (8), 2174-2182.
21. Kuhn, W. *Kolloid-Zeitschrift* **1934,** 68, (1), 2-15.
22. Guth, E.; Mark, H. *Monatshefte für Chemie* **1934,** 65, (1), 93-121.
23. Kuhn, W. *Kolloid-Zeitschrift* **1936,** 76, (3), 258-271.
24. Flory, P. J. *B Am Phys Soc* **1978,** 23, (3), 403-403.
25. Rubinstein, M.; Colby, R. H., *Polymer physics*. Oxford University Press: Oxford, New York, 2003.
26. Stauffer, D.; Coniglio, A.; Adam, M. *Adv Polym Sci* **1982,** 44, 103-158.
27. Eberle, A. P. R.; Castaneda-Priego, R.; Kim, J. M.; Wagner, N. J. *Langmuir* **2012,** 28, (3), 1866-1878.

28. Luo, J. H.; Yuan, G. C.; Zhao, C. Z.; Han, C. C.; Chen, J.; Liu, Y. *Soft Matter* **2015,** 11, (12), 2494-2503.
29. James, H. M.; Guth, E. *J Chem Phys* **1953,** 21, (6), 1039-1049.
30. Gennes, P. G. d., *Scaling concepts in polymer physics*. Cornell University Press: Ithaca, N.Y., 1979; p 324 p.
31. Head, D. A.; Levine, A. J.; MacKintosh, F. C. *Phys Rev Lett* **2003,** 91, (10), 108102.
32. Skouri, R.; Schosseler, F.; Munch, J. P.; Candau, S. J. *Macromolecules* **1995,** 28, (1), 197-210.
33. Rubinstein, M.; Panyukov, S. *Macromolecules* **1997,** 30, (25), 8036-8044.
34. Huang, T.; Xu, H. G.; Jiao, K. X.; Zhu, L. P.; Brown, H. R.; Wang, H. L. *Adv Mater* **2007,** 19, (12), 1622-+.
35. Haraguchi, K.; Takehisa, T. *Adv Mater* **2002,** 14, (16), 1120-1124.
36. Kokabi, M.; Sirousazar, M.; Hassan, Z. M. *Eur Polym J* **2007,** 43, (3), 773-781.
37. Lu, P. J.; Zaccarelli, E.; Ciulla, F.; Schofield, A. B.; Sciortino, F.; Weitz, D. A. *Nature* **2008,** 453, (7194), 499-U4.
38. Bergenholtz, J.; Poon, W. C. K.; Fuchs, M. *Langmuir* **2003,** 19, (10), 4493-4503.
39. Dijkstra, M.; Hansen, J. P.; Madden, P. A. *Phys Rev Lett* **1995,** 75, (11), 2236-2239.
40. Delhorme, M.; Jonsson, B.; Labbez, C. *Soft Matter* **2012,** 8, (37), 9691-9704.
41. Du, F. M.; Scogna, R. C.; Zhou, W.; Brand, S.; Fischer, J. E.; Winey, K. I. *Macromolecules* **2004,** 37, (24), 9048-9055.
42. Zhang, S. J.; Lin, W.; Wong, C. P.; Bucknall, D. G.; Kumar, S. *Acs Appl Mater Inter* **2010,** 2, (6), 1642-1647.
43. Thostenson, E. T.; Ren, Z. F.; Chou, T. W. *Compos Sci Technol* **2001,** 61, (13), 1899-1912.
44. Gojny, F. H.; Wichmann, M. H. G.; Fiedler, B.; Schulte, K. *Compos Sci Technol* **2005,** 65, (15-16), 2300-2313.
45. Parr, R. G., Density Functional Theory of Atoms and Molecules. In *Horizons of Quantum Chemistry: Proceedings of the Third International Congress of Quantum Chemistry Held at Kyoto, Japan, October 29 - November 3, 1979*, Fukui, K.; Pullman, B., Eds. Springer Netherlands: Dordrecht, 1980; pp 5-15.
46. Allen, M. P.; Tildesley, D. J., *Computer simulation of liquids*. Clarendon Press ;

Oxford University Press: Oxford England

New York, 1987; p xix, 385 p.
47. Reddy, J. N.; Gartling, D. K., *The finite element method in heat transfer and fluid dynamics*. 3rd ed.; CRC Press: Boca Raton, FL, 2010; p xxiii, 500 p.
48. Chung, T. *NASA STI/Recon Technical Report A* **1978,** 78, 44102.
49. Chen, S.; Doolen, G. D. *Annu Rev Fluid Mech* **1998,** 30, 329-364.
50. Haile, J. M., *Molecular dynamics simulation : elementary methods*. Wiley: New York, 1992; p xvii, 489 p.
51. Rahman, A. *Phys Rev* **1964,** 136, (2A), A405-A411.
52. Rapaport, D. C., *The art of molecular dynamics simulation*. 2nd ed.; Cambridge University Press: Cambridge, UK ; New York, NY, 2004; p xiii, 549 p.
53. Leach, A. R., *Molecular modelling : principles and applications*. 2nd ed.; Prentice Hall: Harlow, England ; New York, 2001; p xxiv, 744 p., 16 p. of plates.
54. Verlet, L. *Phys Rev* **1967,** 159, (1), 98-103.

55. Swope, W. C.; Andersen, H. C.; Berens, P. H.; Wilson, K. R. *J Chem Phys* **1982,** 76, (1), 637-649.
56. Nosé, S. *Mol Phys* **1984,** 52, (2), 255-268.
57. Grest, G. S.; Kremer, K. *Phys Rev A* **1986,** 33, (5), 3628-3631.
58. Kremer, K.; Grest, G. S.; Carmesin, I. *Phys Rev Lett* **1988,** 61, (5), 566-569.
59. Kremer, K.; Grest, G. S. *J Chem Phys* **1990,** 92, (8), 5057-5086.
60. Duering, E. R.; Kremer, K.; Grest, G. S. *J Chem Phys* **1994,** 101, (9), 8169-8192.
61. Everaers, R.; Kremer, K. *Phys Rev E* **1996,** 53, (1), R37-R40.
62. Everaers, R.; Kremer, K. *Macromolecules* **1995,** 28, (21), 7291-7294.
63. Duering, E. R.; Kremer, K.; Grest, G. S. *Phys Rev Lett* **1991,** 67, (25), 3531-3534.
64. Duering, E. R.; Kremer, K.; Grest, G. S. *Macromolecules* **1993,** 26, (12), 3241-3244.
65. Dunweg, B.; Paul, W. *Int J Mod Phys C* **1991,** 2, (3), 817-827.
66. Schneider, T.; Stoll, E. *Physical Review B* **1978,** 17, (3), 1302-1322.
67. Evans, D. J.; Holian, B. L. *J Chem Phys* **1985,** 83, (8), 4069-4074.
68. http://lammps.sandia.gov/
69. Plimpton, S. *J Comput Phys* **1995,** 117, (1), 1-19.
70. Kopeček, J. *Biomaterials* **2007,** 28, (34), 5185-5192.
71. Hoffman, A. S. *Advanced drug delivery reviews* **2012,** 64, 18-23.
72. Qiu, Y.; Park, K. *Advanced drug delivery reviews* **2012,** 64, 49-60.
73. Haraguchi, K. *Current Opinion in Solid State and Materials Science* **2007,** 11, (3), 47-54.
74. Schexnailder, P.; Schmidt, G. *Colloid and Polymer Science* **2009,** 287, (1), 1-11.
75. Zhang, L.; Shi, G. *The Journal of Physical Chemistry C* **2011,** 115, (34), 17206-17212.
76. Liu, Y.; Zhu, M.; Liu, X.; Zhang, W.; Sun, B.; Chen, Y.; Adler, H.-J. P. *Polymer* **2006,** 47, (1), 1-5.
77. Haraguchi, K.; Ebato, M.; Takehisa, T. *Adv Mater* **2006,** 18, (17), 2250-2254.
78. Haraguchi, K.; Takehisa, T.; Fan, S. *Macromolecules* **2002,** 35, (27), 10162-10171.
79. Rao, Y. Q. *Polymer* **2007,** 48, (18), 5369-5375.
80. Xu, Y.; Wu, Q.; Sun, Y.; Bai, H.; Shi, G. *ACS nano* **2010,** 4, (12), 7358-7362.
81. Cong, H.-P.; Ren, X.-C.; Wang, P.; Yu, S.-H. *ACS nano* **2012,** 6, (3), 2693-2703.
82. Haraguchi, K. *Polym J* **2011,** 43, (3), 223-241.
83. Haraguchi, K.; Li, H. J. *Angew Chem Int Edit* **2005,** 44, (40), 6500-6504.
84. Haraguchi, K. *Curr Opin Solid St M* **2007,** 11, (3-4), 47-54.
85. Haraguchi, K.; Takehisa, T. *Adv Mater* **2002,** 14, (16), 1120.
86. Haraguchi, K.; Takehisa, T.; Fan, S. *Macromolecules* **2002,** 35, (27), 10162-10171.
87. Haraguchi, K.; Farnworth, R.; Ohbayashi, A.; Takehisa, T. *Macromolecules* **2003,** 36, (15), 5732-5741.
88. Haraguchi, K.; Farnworth, R.; Ohbayashi, A.; Takehisa, T. *Macromolecules* **2003,** 36, (15), 5732-5741.
89. Shibayama, M.; Suda, J.; Karino, T.; Okabe, S.; Takehisa, T.; Haraguchi, K. *Macromolecules* **2004,** 37, (25), 9606-9612.
90. Shibayama, M.; Karino, T.; Miyazaki, S.; Okabe, S.; Takehisa, T.; Haraguchi, K. *Macromolecules* **2005,** 38, (26), 10772-10781.
91. Haraguchi, K.; Li, H. J. *Macromolecules* **2006,** 39, (5), 1898-1905.
92. Miyazaki, S.; Karino, T.; Endo, H.; Haraguchi, K.; Shibayama, M. *Macromolecules* **2006,** 39, (23), 8112-8120.

93. Haraguchi, K.; Li, H. J.; Song, L. Y.; Murata, K. *Macromolecules* **2007,** 40, (19), 6973-6980.
94. Haraguchi, K.; Uyama, K.; Tanimoto, H. *Macromol Rapid Comm* **2011,** 32, (16), 1253-1258.
95. Haraguchi, K. *J Stem Cells Regen Med* **2012,** 8, (1), 2-11.
96. Aalaie, J.; Youssefi, M. *J Macromol Sci B* **2012,** 51, (6), 1027-1040.
97. Rao, Y. Q.; Pochan, J. M. *Macromolecules* **2007,** 40, (2), 290-296.
98. Nie, J. J.; Du, B. Y.; Oppermann, W. *Macromolecules* **2005,** 38, (13), 5729-5736.
99. Nie, J.; Du, B.; Oppermann, W. *The Journal of Physical Chemistry B* **2006,** 110, (23), 11167-11175.
100. Delhorme, M.; Labbez, C.; Jonsson, B. *J Phys Chem Lett* **2012,** 3, (10), 1315-1320.
101. Kumar, S. K.; Panagiotopoulos, A. Z. *Phys Rev Lett* **1999,** 82, (25), 5060.
102. Corezzi, S.; De Michele, C.; Zaccarelli, E.; Tartaglia, P.; Sciortino, F. *The Journal of Physical Chemistry B* **2009,** 113, (5), 1233-1236.
103. Balazs, A. C.; Anderson, C.; Muthukumar, M. *Macromolecules* **1987,** 20, (8), 1999-2003.
104. Baljon, A. R.; Flynn, D.; Krawzsenek, D. *The Journal of chemical physics* **2007,** 126, (4), 044907.
105. Kumar, S. K.; Douglas, J. F. *Phys Rev Lett* **2001,** 87, (18).
106. Vernon, D.; Plischke, M.; Joos, B. *Phys Rev E* **2001,** 64, (3).
107. Hou, J. X.; Svaneborg, C.; Everaers, R.; Grest, G. S. *Phys Rev Lett* **2010,** 105, (6).
108. Erpenbeck, J. J. *Phys Rev A* **1987,** 35, (1), 218-232.
109. Jones, R. E.; Mandadapu, K. K. *The Journal of chemical physics* **2012,** 136, (15), 154102.
110. Del Gado, E.; Fierro, A.; de Arcangelis, L.; Coniglio, A. *Phys Rev E* **2004,** 69, (5), 051103.
111. Kumar, S. K.; Douglas, J. F. *Phys Rev Lett* **2001,** 87, (18), 188301.
112. Xu, D.; Bhatnagar, D.; Gersappe, D.; Sokolov, J. C.; Rafailovich, M. H.; Lombardi, J. *Macromolecules* **2015,** 48, (3), 840-846.
113. Paul, D. R., *Polymer blends*. Elsevier: 2012; Vol. 1.
114. Gan, Z.; Yu, D.; Zhong, Z.; Liang, Q.; Jing, X. *Polymer* **1999,** 40, (10), 2859-2862.
115. Wu, S. *Polymer* **1985,** 26, (12), 1855-1863.
116. Gazotti Jr, W.; Casalbore-Miceli, G.; Mitzakoff, S.; Geri, A.; Gallazzi, M.; De Paoli, M.-A. *Electrochimica acta* **1999,** 44, (12), 1965-1971.
117. Mano, J.; Koniarova, D.; Reis, R. *Journal of Materials Science: Materials in Medicine* **2003,** 14, (2), 127-135.
118. Lizymol, P.; Thomas, S. *Polymer degradation and stability* **1993,** 41, (1), 59-64.
119. Porter, R. S.; Wang, L. H. *Polymer* **1992,** 33, (10), 2019-2030.
120. Elias, L.; Fenouillot, F.; Majesté, J.-C.; Alcouffe, P.; Cassagnau, P. *Polymer* **2008,** 49, (20), 4378-4385.
121. Chen, C. C.; White, J. L. *Polymer Engineering & Science* **1993,** 33, (14), 923-930.
122. Ray, S. S.; Bousmina, M. *Macromol Rapid Comm* **2005,** 26, (20), 1639-1646.
123. Si, M.; Araki, T.; Ade, H.; Kilcoyne, A.; Fisher, R.; Sokolov, J. C.; Rafailovich, M. H. *Macromolecules* **2006,** 39, (14), 4793-4801.
124. Cao, Y. W.; Zhang, J.; Feng, J. C.; Wu, P. Y. *Acs Nano* **2011,** 5, (7), 5920-5927.
125. Yousfi, M.; Soulestin, J.; Vergnes, B.; Lacrampe, M. F.; Krawczak, P. *Macromol Mater Eng* **2013,** 298, (7), 757-770.

126. Chremos, A.; Nikoubashman, A.; Panagiotopoulos, A. Z. *The Journal of chemical physics* **2014,** 140, (5), 054909.
127. Brochard, F.; De Gennes, P. *Langmuir* **1992,** 8, (12), 3033-3037.
128. Goveas, J.; Fredrickson, G. *The European Physical Journal B-Condensed Matter and Complex Systems* **1998,** 2, (1), 79-92.
129. Adhikari, N.; Goveas, J. *Journal of Polymer Science Part B: Polymer Physics* **2004,** 42, (10), 1888-1904.
130. Barrat, J.-L.; Bocquet, L. *Phys Rev Lett* **1999,** 82, (23), 4671.
131. Zhao, R.; Macosko, C. W. *Journal of Rheology (1978-present)* **2002,** 46, (1), 145-167.
132. Nijmeijer, M.; Bakker, A.; Bruin, C.; Sikkenk, J. *The Journal of chemical physics* **1988,** 89, (6), 3789-3792.
133. Cai, Y.; Wu, H.; Luo, S. *The Journal of chemical physics* **2014,** 140, (21), 214317.
134. Chapin, D. M.; Fuller, C.; Pearson, G. *Journal of Applied Physics* **1954,** 25, (5), 676-677.
135. Bohannon, J. *Science* **2007,** 315, (5813), 792-792.
136. Shrotriya, V. *Nat Photonics* **2009,** 3, (8), 447-449.
137. Swanson, R. M. *Science* **2009,** 324, (5929), 891-892.
138. Shah, A.; Torres, P.; Tscharner, R.; Wyrsch, N.; Keppner, H. *science* **1999,** 285, (5428), 692-698.
139. Lewis, N. S. *science* **2007,** 315, (5813), 798-801.
140. Gabor, N. M.; Zhong, Z.; Bosnick, K.; Park, J.; McEuen, P. L. *Science* **2009,** 325, (5946), 1367-1371.
141. Zhu, Z.; Waller, D.; Gaudiana, R. *Journal of Macromolecular Science, Part A* **2007,** 44, (12), 1249-1253.
142. Currie, M. J.; Mapel, J. K.; Heidel, T. D.; Goffri, S.; Baldo, M. A. *Science* **2008,** 321, (5886), 226-228.
143. Datta, D.; Kumar, S. *Journal of Applied Physics* **2009,** 106, (7), 074517.
144. Riedel, I.; Dyakonov, V. *physica status solidi (a)* **2004,** 201, (6), 1332-1341.
145. Dennler, G.; Scharber, M. C.; Brabec, C. J. *Adv Mater* **2009,** 21, (13), 1323-1338.
146. Lee, C.-K.; Pao, C.-W.; Chu, C.-W. *Energy & Environmental Science* **2011,** 4, (10), 4124-4132.
147. Pan, C.; Li, H.; Akgun, B.; Satijia, S. K.; Zhu, Y.; Xu, D.; Ortiz, J.; Gersappe, D.; Rafailovich, M. H. *Macromolecules* **2013,** 46, (5), 1812-1819.